Journal of Computational Physics 229 (2010) 5090–5122

Contents lists available at ScienceDirect

Journal of Computational Physics

journal homepage: www.elsevier.com/locate/jcp

Curvilinear finite-volume schemes using high-order compact interpolation

Arnaud Fosso P. [a,*], Hugues Deniau [a], Frédéric Sicot [a], Pierre Sagaut [b]

[a] CERFACS, CFD Team, 42 avenue Gaspard Coriolis, 31057 Toulouse cedex, France
[b] Institut Jean Le Rond d'Alembert, Université Pierre et Marie Curie (UPMC), 4 place Jussieu – case 162, F-75252 Paris cedex 5, France

ARTICLE INFO

Article history:
Received 15 September 2009
Received in revised form 19 March 2010
Accepted 22 March 2010
Available online 30 March 2010

Keywords:
Finite-volume
High-order scheme
Compact interpolation
Multiblock computations
Stability analysis
Aeroacoustics

ABSTRACT

During the last years, the need of high fidelity simulations on complex geometries for aeroacoustics predictions has grown. Most of high fidelity numerical schemes, in terms of low dissipative and low dispersive effects, lie on finite-difference (FD) approach. But for industrial applications, FD schemes are less robust compared to finite-volume (FV) ones. Thus the present study focuses on the development of a new compact FV scheme for two- and three-dimensional applications.

The proposed schemes are formulated in the physical space and not in the computational space as it is the case in most of the known works. Therefore, they are more appropriate for general grids. They are based on compact interpolation to approximate interface-averaged field values using known cell-averaged values. For each interface, the interpolation coefficients are determined by matching Taylor series expansions around the interface center. Two types of schemes can be distinguished. The first one uses only the curvilinear abscissa along a mesh line to derive a sixth-order compact interpolation formulae while the second, more general, uses coordinates in a spatial three-dimensional frame well chosen. This latter is formally sixth-order accurate in a preferred direction almost orthogonal to the interface and at most fourth-order accurate in transversal directions.

For non-linear problems, different approaches can be used to keep the high-order scheme. However, in the present paper, a MUSCL-like formulation was sufficient to address the presented test cases.

All schemes have been modified to treat multiblock and periodic interfaces in such a way that high-order accuracy, stability, good spectral resolution, conservativeness and low computational costs are guaranteed. This is a first step to insure good scalability of the schemes although parallel performances issues are not addressed. As high frequency waves, badly resolved, could be amplified and then destabilize the scheme, compact filtering operators have been used.

Numerous test cases as the linear convection of a Gaussian wave, the convection of a Lamb–Oseen vortex and the diffraction of an acoustic wave on a plane have been realized to validate the schemes. The most efficient schemes are shown to be at least fifth-order accurate on linear and non-linear convection problems. They are also less dissipative and less dispersive on non-uniform curvilinear grids than schemes using implicit interpolation with constant coefficients of the same order on uniform cartesian grids.

1. Introduction

The use of computational fluid dynamics (CFD) methods in computational aeroacoustics (CAA) to address noise generation and propagation problems is now a well established practice in engineering. However it is well known that CFD methods

* Corresponding author. Tel.: +33 5 61 19 30 65; fax: +33 5 61 19 30 00.
E-mail address: fosso@cerfacs.fr (Arnaud Fosso P.).

0021-9991/$ - see front matter © 2010 Elsevier Inc. All rights reserved.
doi:10.1016/j.jcp.2010.03.027

must be modified in order to satisfy stringent requirements of CAA [23]. Indeed, aeroacoustics problems generally display an unsteady behaviour, a broad and disparate spectral bandwidth along with a large-magnitude disparity between the mean and acoustic flow quantities. Thus, important efforts have been done to realize numerical schemes higher-order accurate, low dissipative and low dispersive.

Numerous studies have contributed to improve numerical tools for aeroacoustic computation but almost entirely in finite-difference (FD) framework. The main ideas of those works are illustrated by the Tam and Webb [25] dispersion relation preserving (DRP) scheme and the Padé-like compact schemes [14]. These methods exhibit an improved spectral resolution while having the same accuracy as the standard explicit methods of the same order. One can find abundant literature on the application of these methods on arbitrary meshes always in the FD context [5,26].

However finite-volume (FV) formulations are generally preferred for industrial applications due to their robustness. Indeed, they are based on the weak formulation of the field equations and so require less smoothness of functions or mesh than FD formulations. Furthermore, FV methods are advantageous since they allow to satisfy the governing conservation laws of the fluid physics. Actually, it is shown in Mattiussi [15], using algebraic topology concepts, that integral methods like FV and FE (finite element) methods are more suitable for field equations than FD methods. Therefore, the need of high-order accurate and low dissipative and low dispersive FV schemes on arbitrary grids is certain, and the present study is in line with this approach.

Efforts have been done to extend both DRP and compact schemes approaches to FV context. For example, Gaitonde and Shang [3] introduced a class of fourth-order FV compact schemes for linear problems. Kobayashi [12] extends this work by analyzing general implicit interpolation schemes. Nance et al. [16] proposed a way to set up explicit interpolation which satisfies the DRP property to calculate rotorcraft noise. Recently, Popescu et al. [21] adapted DRP scheme of Tam and optimized prefactored compact schemes of Ashcroft and Zhang [1] and Hixon [10] to obtain high-order, low dissipative and dispersive FV schemes. But all these works deal with uniform grids. Pereira et al. [17] performed computations for incompressible Navier–Stokes equations using a fourth-order compact FV scheme. They extend the scheme to arbitrary grids using transformed coordinates. The same approach has been used in the recent work of Piller and Stalio [18,19]. They take into account that, in FV context, cell-averaged values are known and in particular they do not use these value as pointwise values at cells centers. Lacor et al. [13] proposed a compact interpolation of values on cell interfaces in the physical space and these values are used to determine the fluxes. This interpolation is made by directly accounting for multidimensional derivatives involving in the Taylor series expansion of the function to interpolate. The scheme obtained were fourth-order accurate on regular grids and second-order accurate on arbitrary grids. This approach is well suited for highly irregular grids.

This study is in line with the one of Lacor and coworkers. The proposed schemes allow to reach, on average, the fifth-order accuracy on regular meshes (even curvilinear) and the spectral resolution of commonly used FD compact schemes on a cartesian uniform mesh. To do that, they use sixth-order compact interpolation to compute values on interfaces. The schemes explicitly care that there are cell-averaged values which are used in a FV context. Two types of schemes can be distinguished. The first type uses curvilinear abscissa assuming that the problem is unidimensional (1D) along the curvilinear line between the centers of interfaces on a given mesh line. Therefore, values on interfaces are considered as values at the center of the interface and cell-averaged values are line-averaged values. The second one is more general since it takes into account that values needed on interfaces are interface-averaged values. So they are line-averaged values in 2D and surface-averaged values in 3D. And cell-averaged values are surface-averaged values in 2D and volume-averaged values in 3D. Therefore the Taylor expansion series used to find the interpolation formulae involves multidimensional derivatives.

For aeroacoustics computations, even if the numerical scheme has good properties in terms of dissipation and dispersion, the grid must be fine enough to resolve well either the turbulent structures which are the noise source, and the convection of acoustic wave with a sufficient number of points per wave-length. The number of points is generally so important that computations have to be done with a parallel multiblock strategy. Thus the proposed schemes have to be adapted for multiblock computations and this issue is carefully addressed. Since it is shown that all boundary treatments can create spurious high frequency waves numerical, stabilization procedures are also considered.

The paper is organized as follows. In Section 2, the two types of interior schemes are detailed. After a rapid recall about how a scheme could be studied with the matrix method in Section 2.4, multiblock and periodic boundary closures are discussed in Section 2.5. In Section 3 are reported some remarks specific to the non-linear case. Section 4 gives a rapid view about filtering operators used. Then some numerical tests are performed in Section 5. Firstly, a numerical study is done on a linear convection problem in Section 5.1. Then, a non-linear case which consists in the convection of a vortex, is presented in Section 5.2. Finally, to highlight the high accuracy and the good spectral properties of the schemes, a benchmark acoustic problem is solved in Section 5.3 on an irregular mesh using a non-linear code.

2. Finite-volume method and high-order compact interpolations

Let be considered the following linear convection equation:

$$\frac{\partial u}{\partial t} + \nabla \cdot \mathbf{f}(u) = 0, \tag{1}$$

where $\mathbf{f}(u)$ is a linear vectorial function of u. By integrating Eq. (1) over a volume control Ω and using the Stokes formula, one can obtain:

$$V\frac{\mathrm{d}\bar{u}}{\mathrm{d}t}+\oint_{\partial\Omega}\mathbf{f}(u)\cdot\mathbf{n}\,\mathrm{d}S=0, \tag{2}$$

with $V=|\Omega|$ and

$$\bar{u}=\frac{1}{V}\int_{\Omega}u\,\mathrm{d}\Omega.$$

Now, it is assumed that Ω is a polyhedron (polygon in 2D), *i.e.* the unitary normal on each of its faces is constant over the face. Therefore, using the linearity of $\mathbf{f}$, Eq. (2) leads to:

$$V\frac{\mathrm{d}\bar{u}}{\mathrm{d}t}+\sum_{i=1}^{n_f}\mathbf{f}\left(\int_{\partial\Omega_i}u\,\mathrm{d}S\right)\cdot\mathbf{n}_i=0, \tag{3}$$

where n_f is the number of faces and $\partial\Omega_i$, the ith face of Ω. Eq. (3) is equivalent to

$$V\frac{\mathrm{d}\bar{u}}{\mathrm{d}t}+\sum_{i=1}^{n_f}\mathbf{f}(\tilde{u}_i)S_i\cdot\mathbf{n}_i=0, \tag{4}$$

where $S_i=|\partial\Omega_i|$ and

$$\tilde{u}_i=\frac{1}{S_i}\int_{\partial\Omega_i}u\,\mathrm{d}S.$$

Hence, to obtain a high-order discretization of Eq. (4), it is sufficient to have a high-order approximation of the face-averaged quantity $\tilde{u}_i$.

Now, a three-dimensional structured (indexed by (i,j,k)) grid composed of hexahedrons is considered. This section presents the different strategies proposed to approximate at a high-order the interface-averaged value of a quantity u on the interface $(i+1/2,j,k)$, using cell-averaged values of neighbouring cells. In this section, the mesh line (j,k) for which these two indexes remain constant is under consideration. To make this approximation spatially implicit or compact, the formula involves averaged values on neighbouring interfaces $(i-1/2,j,k)$ and $(i+3/2,j,k)$. Thus the compact interpolation reads as

$$\alpha\tilde{u}_{i-1/2,j,k}+\tilde{u}_{i+1/2,j,k}+\beta\tilde{u}_{i+3/2,j,k}=\sum_{l=-m}^{l=n}\sum_{p=-q}^{p=r}\sum_{s=-t}^{s=u}a_{l,p,s}\bar{u}_{i+l,j+p,k+s}, \tag{5}$$

where

$$\bar{u}_{i,j,k}=\frac{1}{V_{i,j,k}}\int_{V_{i,j,k}}u\,\mathrm{d}V, \tag{6}$$

are cell-averaged values and

$$\tilde{u}_{i+1/2,j,k}\approx\frac{1}{S_{i+1/2,j,k}}\int_{S_{i+1/2,j,k}}u\,\mathrm{d}S, \tag{7}$$

approximate interface-averaged values. The interpolation coefficients α, β and $a_{l,p,s}$ are chosen, depending on the interface $(i+1/2,j,k)$, in order to obtain a given order of approximation.

The system of equations formed with Eq. (5) along the mesh line (j,k) to compute values at the interfaces is a tridiagonal system. This choice has been made since this system is efficiently inversed using, for example, the Thomas algorithm. Moreover, the inversion of the system could be done for each grid line in each dimension.

To determine the interpolation coefficients, a Taylor series expansion is done for each term in Eq. (5), and two possibilities are studied in this paper depending on the following choice:

- u is considered as a function of s, the curvilinear abscissa along the (j,k) line;
- u is considered as a function in a well chosen tridimensional coordinates system (x',y',z').

2.1. Cartesian-like scheme using curvilinear abscissa

In this section, u is assumed to be a function just of the curvilinear abscissa s along (j,k)-line. Such a scheme will be referred to as a cartesian-like scheme in the following.

To obtain a formally sixth-order scheme, Eq. (5) can be reduced as follows:

$$\alpha\tilde{u}_{i-1/2,j,k}+\tilde{u}_{i+1/2,j,k}+\beta\tilde{u}_{i+3/2,j,k}=a\bar{u}_{i-1,j,k}+b\bar{u}_{i,j,k}+c\bar{u}_{i+1,j,k}+d\bar{u}_{i+2,j,k}. \tag{8}$$

A Taylor series expansion of $u(s)$ about the center of the interface $(i+1/2,j,k)$ is done for all terms in Eq. (8). In order to get the sixth-order, it is necessary to match left and right hand sides coefficients of successive derivatives ∂s^q up to the fifth-order.

So, six equations are obtained, and coefficients α, β, a, b, c and d, are explicitly found as functions of the distances between interfaces (Fig. 1) which represent the curvilinear abscissae. (see details in Appendix A).

For an uniform grid, one can find the following interpolation formula:

$$\frac{1}{3}\tilde{u}_{i-1/2,j,k}+\tilde{u}_{i+1/2,j,k}+\frac{1}{3}\tilde{u}_{i+3/2,j,k}=\frac{1}{36}\bar{u}_{i-1,j,k}+\frac{29}{36}\bar{u}_{i,j,k}+\frac{29}{36}\bar{u}_{i+1,j,k}+\frac{1}{36}\bar{u}_{i+2,j,k}. \tag{9}$$

However, this scheme does not account for the variation of the cells and interfaces shapes and for the curvature of mesh lines. This deficiency is corrected by a more general approach presented in the next section.

2.2. General curvilinear scheme

In the general case, since u is a function of three coordinates x, y, z for three-dimensional flow, the Taylor series expansion introduced in Eq. (5) involves all derivatives with respect to these three directions:

$$u(x,y,z)=\sum_{m=0}^{\infty}\sum_{n=0}^{\infty}\sum_{p=0}^{\infty}\frac{1}{m!}\frac{1}{n!}\frac{1}{p!}(x-x_0)^m(y-y_0)^n(z-z_0)^p\frac{\partial^{m+n+p}u}{\partial x^m\partial y^n\partial z^p}(x_0,y_0,z_0). \tag{10}$$

Remembering that averaged values as defined by Eqs. (6) and (7) are considered, relations obtained using the Taylor series expansion involve kinetic moments $f_\Omega^{x^m y^n z^p}=\int_\Omega (x-x_\Omega)^m(y-y_\Omega)^n(z-z_\Omega)^p\,\mathrm{d}\Omega$ of cells and interfaces which belong to the stencil (see Appendices B and C for details).

In the two-dimensional case, there are 21 relations to satisfy in order to get a sixth-order scheme (see Table 1) and it would be too expensive to use a suitable stencil to fullfill these relations.

In a previous study, Lacor et al. [13] proposed to use supplementary cells above and below the interface (see Fig. 2) to obtain a fourth-order scheme. As the number of coefficients was still not sufficient (8 coefficients for 10 equations to obtain the fourth-order), they proposed, in a second step to obtain a formally third-order accurate scheme (six equations) by imposing all the derivatives up to the second-order to be cancelled out and minimizing the third derivatives coefficients with a least square method. Since this method leads to unstable simulations, they reduced the formal order to two and set $\alpha=\beta=1/4$ which are the values obtained to get the fourth-order accuracy on an uniform grid.

The general compact FV approach proposed in the present work also relies on the use of supplementary cells above and below the interface and a least square approach to account for their contribution. But it differs from Lacor's method on some important points. The main idea lies in the definition of a new frame, local to each interface, in which the Taylor series expansions are performed. Since only the interfaces $(i-1/2,j,k)$, $(i+1/2,j,k)$ and $(i+3/2,j,k)$ appear in Eq. (5), the proposed scheme has already a preferred direction along this (j,k)-line. Thus a new frame (x',y',z') is introduced so that the x'-direction represents this preferred direction, tangent to (j,k) mesh line. Taylor series expansions are written in this frame, and all derivatives along x' are cancelled out in order to get the sixth-order accuracy in this direction. Transverse derivatives along

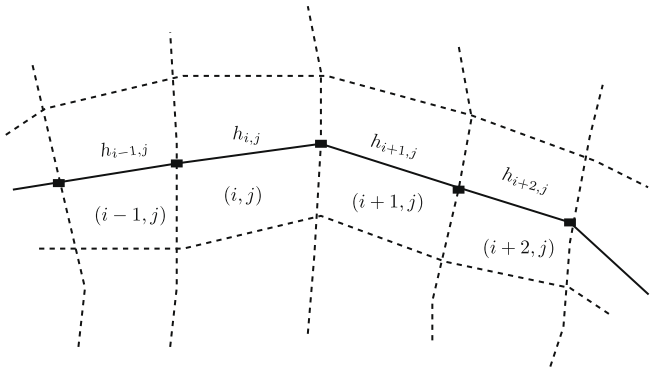

Fig. 1. Cartesian-like scheme using curvilinear distances between interfaces.

Table 1
Derivatives to cancel out in order to get a formal sixth-order interpolation in all directions.

	Derivatives	Total number
1D	$\partial^{(0)},\partial^i x^i,\ i=1,\ldots,5$	6
2D	$\partial^{(0)},\partial^{i+j}x^iy^j,\ i,j\in\{0,\ldots,5\},\ i+j\leqslant 5$	21
3D	$\partial^{(0)},\partial^{i+j+k}x^iy^jz^k,\ i,j,k\in\{0,\ldots,5\},\ i+j+k\leqslant 5$	56

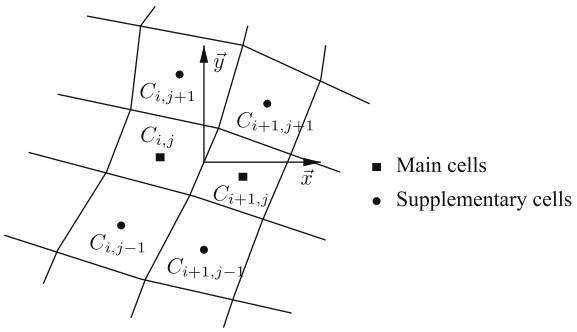

Fig. 2. Cells used by Lacor et al. for the curvilinear interpolation.

y' and z' are accounted for as corrections terms using a least square approach. Before presenting these so called transverse correction, the local frame definition is addressed.

2.2.1. Local reference frame

Three types of local frames have been considered. The first and second type are orthogonal and differ by the definition of the preferred direction x'. For the first type, this direction is defined as the direction given by the centers of the two cells adjacent to the central interface of the stencil (see Fig. 3(a)). For the second one, the x' direction is defined as the normal to the central interface (Fig. 3(b)). For both types, the two other directions are built as two independent vectors in the plane normal to x'.

The third frame is non-orthogonal. Its x' axis is chosen as for the first type, the y' and z' directions correspond to the mesh lines which link the interface center in j and k directions as presented in Fig. 3(c). The y' direction corresponds to the line which joins the $I_{i+1/2,j+1}$ and $I_{i+1/2,j-1}$ points ($I_{i+1/2,j}$ is the center of the $S_{i+1/2,j}$ interface). The relevance of this frame will clearly appear when the discretization stencil will be shown.

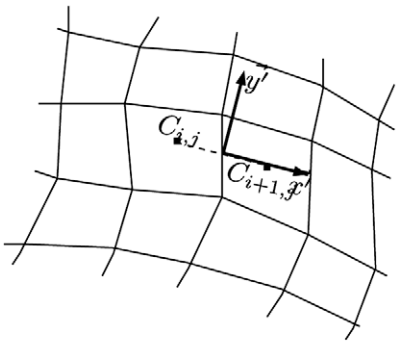

(a) Orthogonal frame defined by the cell centers line

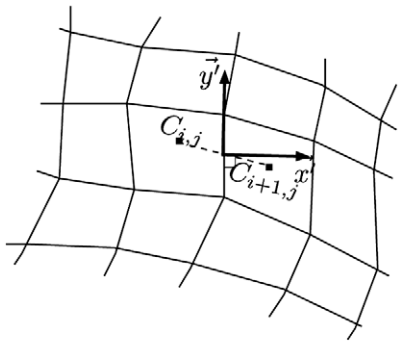

(b) Orthogonal frame defined by the normal of the interface

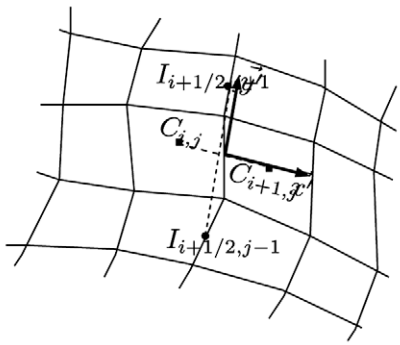

(c) Non orthogonal frame defined by the cell centers lines

Fig. 3. Different local frames considered for the high-order curvilinear interpolation.

2.2.2. Transverse derivatives and discretization stencil

Since it is too expensive to extend the stencil so that all transverse derivatives are cancelled, it was initially decided to account for the first- and second-order transverse derivatives. But in 2D, for example, it amounts to cancel $\partial y'$, $\partial x'y'$, $\partial y''^2$ derivatives only and to achieve that, only three supplementary cells are needed. Adding only three supplementary cells breaks the symmetry of the stencil, and such a symmetry-breaking may render the preservation of the spectral resolution of the scheme more difficult. Therefore, it was decided to account for all transverse derivatives up to the fourth-order ($\partial y'$, $\partial x'y'$, $\partial y'^2$, $\partial x'^2y'$, $\partial x'y'^2$, and $\partial y'^3$) and to use four supplementary cells as Lacor et al. in 2D case (eight supplementary cells in 3D). The list of all derivatives used are presented in Table 2. Fig. 4 presents the resulting stencil in 2D case. The four points represented by a square are used to match the derivatives in x' direction, and the four points represented by a circle (•) are used for transversal correction.

As it can be seen in Fig. 5, the two local frames (x',y') and (x'',y'') corresponding to the first and the third local reference frames presented respectively, directly influence the transverse correction. In fact, the four points (•) constitute a better stencil to approximate the derivative in the y'' direction than in the y' one.

2.2.3. Least-square error minimization

However, at this point, in 2D for example, there are four supplementary coefficients than in the cartesian case and up to six supplementary relations to verify (see Table 2). So the final system is overdefined. Those six relations (sixteen in 3D), are minimized by a least square approach but with a weighting distribution in order to give different importance to the contribution of the different transverse derivatives. In particular, it has been numerically observed that the weighting coefficients

Table 2
Derivatives used for the general curvilinear scheme.

Dimension	Derivatives	Total number
2D	$\partial^{(0)}$, $\partial x'$, $\partial^2 x'^2$, $\partial^3 x'^3$, $\partial^4 x'^4$, $\partial^5 x'^5$, $\partial y'$, $\partial^2 y'^2$, $\partial^2 x'y'$, $\partial^3 y'^3$, $\partial^3 x'^2y'$, $\partial^3 x'y'^2$	12
3D	$\partial^{(0)}$, $\partial x'$, $\partial^2 x'^2$, $\partial^3 x'^3$, $\partial^4 x'^4$, $\partial^5 x'^5$, $\partial y'$, $\partial z'$, $\partial^2 y'^2$, $\partial^2 z'^2$, $\partial^2 x'y'$, $\partial^2 x'z'$, $\partial^2 y'z'$, $\partial^3 y'^3$, $\partial^3 z'^3$, $\partial^3 x'^2y'$, $\partial^3 x'y'^2$, $\partial^3 x'^2z'$, $\partial^3 x'z'^2$, $\partial^3 y'^2z'$, $\partial^3 y'z'^2$, $\partial^3 x'y'z'$	22

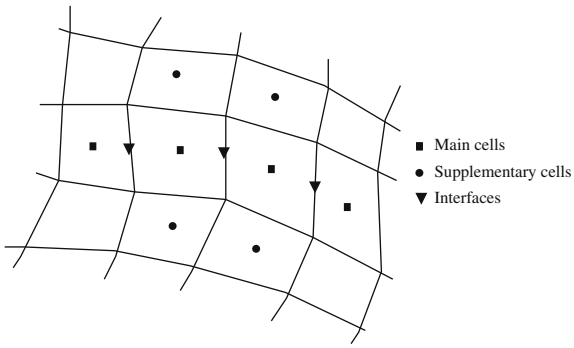

Fig. 4. Cells used by the curvilinear interpolation.

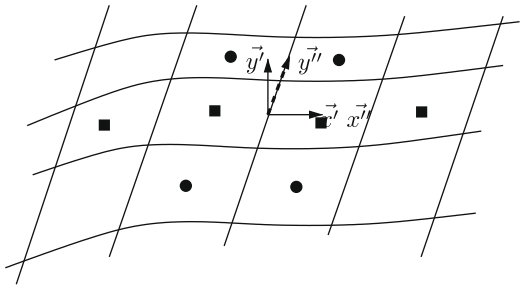

Fig. 5. Local frame and discretization stencil.

relative to the first and second-order derivatives must be larger than those relative to higher-order ones to get the best dissipation and dispersion properties.

For sake of simplicity, the 2D case is considered. The interpolation equation reads:

$$\alpha\tilde{u}_{i-1/2,j}+\tilde{u}_{i+1/2,j}+\beta\tilde{u}_{i+3/2,j}=a\bar{u}_{i-1,j}+b\bar{u}_{i,j}+c\bar{u}_{i+1,j}+d\bar{u}_{i+2,j}+e\bar{u}_{i,j-1}+f\bar{u}_{i,j+1}+g\bar{u}_{i+1,j-1}+h\bar{u}_{i+1,j+1}. \tag{11}$$

The unknown coefficients are separated as $X=(\underbrace{\alpha,\beta,a,b,c,d}_{X_1}\ \underbrace{e,f,g,h}_{X_2})$. The final system obtained could be written

$$M.X=\begin{pmatrix}A & B\\ A' & B'\end{pmatrix}\left|\begin{matrix}X_1\\ X_2\end{matrix}\right.=\left|\begin{matrix}C\\ C'\end{matrix}\right., \tag{12}$$

where A is a 6×6 matrix and B' a 6×4 matrix. $(A\quad B)$ are the relations cancelling all derivatives in the principal direction, and $(A'\quad B')$ are the relations cancelling all transverse derivatives. These matrix are normalized so that, the maximum coefficient of each line equals 1, *i.e.*

$$\max_j(M_{ij})=1,\ \forall i.$$

The part $(A\quad B)$ of the system must mainly define X_1, so it is not solved by the least square approach. Thus, the final system is

$$\begin{pmatrix}I & 0\\ 0 & \widetilde{B}^T\end{pmatrix}\begin{pmatrix}A & B\\ A' & B'\end{pmatrix}\left|\begin{matrix}X_1\\ X_2\end{matrix}\right.=\begin{pmatrix}I & 0\\ 0 & \widetilde{B}^T\end{pmatrix}\left|\begin{matrix}C\\ C'\end{matrix}\right., \tag{13}$$

where, $\widetilde{B}$ is the matrix with rows defined as

$$L_i(\widetilde{B})=\omega_i L_i(B'). \tag{14}$$

with $L_i(B)$ which is the ith row of the matrix B and ω_i a weight defining how much better than other the transverse derivative corresponding to the ith row must be cancelled.

2.3. Remarks

One can remark that for cartesian meshes, both approaches (the one using transverse derivatives and the one using the curvilinear abscissa) match (it is proved in Appendix A).

The final compact formula is not directly applicable to boundaries of a closed domain. It is therefore necessary to set up a different scheme for boundaries and this is done in Section 2.5.

To ensure that the tridiagonal matrix obtained with Eq. (8) is inversible, it is checked that it is diagonally dominant *i.e.*:

$$|\alpha|+|\beta|\leqslant 1,$$

otherwise, α and β are arbitrarily set to 1/3, thus the order is reduced to four. This generally happens when the mesh is strongly stretched or distorted. In this work, this situation happened, for example, when performing the linear convection on a 3D randomly perturbed mesh (see results presented in Section 5.1.5).

2.4. Eigenvalues and spectral resolution

The spectral behaviour of the proposed schemes is now analyzed considering the 1D linear convection equation:

$$\frac{\partial u}{\partial t}+\frac{\partial u}{\partial x}=0. \tag{15}$$

The discretization of Eq. (15) by a FV method could be written in a FD-like matrix form:

$$\frac{\mathrm{d}}{\mathrm{d}t}\overline{U}=L\overline{U}, \tag{16}$$

where L is the space discretization operator (which discretizes the continuous operator $-\partial_x$) and $\overline{U}$ the vector of the cell-averaged values. The space discretization operator L is said to be stable if $\mathrm{Re}(\lambda)\leqslant 0$, for any eigenvalue λ of L.

To study the spectral resolution of the scheme, an uniform 1D discretization of size h is considered, along with the following propagating wave solution:

$$u^k(x,t)=U^k e^{I(kx-\omega t)}. \tag{17}$$

One can show that, if the sixth-order compact interpolation is used on all points:

$$\bar{u}_i'^k=(L\overline{U})_i=Ik'\bar{u}_i^k, \tag{18}$$

where k' is the modified wavenumber associated with the numerical scheme. Using the FD-like form of the scheme, one can find that k' is a real number and the scheme has the same spectral properties as the Lele's tridiagonal sixth-order compact scheme [14].

However, when a different scheme is applied on boundaries, the modified wavenumber differs on each point. To compute this local modified wavenumber, it is necessary to use the matrix form Eq. (16). One can write

$$\overline{U}'^{k} = L\overline{U}^{k} = IK'\overline{U}^{k}, \tag{19}$$

where K' is the diagonal matrix formed by the local modified wavenumber k'_i of each cell i. This local k'_i is very close to the one defined by Eq. (18) in the interior of the domain. On boundaries, k'_i is generally no longer real. The imaginary part introduces either a dissipative or an anti-diffusive effect. More precisely, a positive imaginary part corresponds to an anti-diffusion (amplification) since the wave propagate from the left to the right. Thus the study of this local modified wavenumber on boundaries as proposed by Sengupta et al. [22] gives a view of the spectral resolution and the local stability of the scheme at boundaries.

The next section presents some boundary closures at the interface boundary between two blocks. Firstly, a numerical study of eigenvalues of the space semi-discretization operator L gives a view of the global stability of the scheme. Then, a numerical study of local modified wavenumbers gives information about the spectral resolution and the local stability of the scheme at boundaries.

2.5. Multiblock and periodic boundaries

Since the aim of this work is to set up high-order compact FV method for multiblock computations, a particular attention is paid to multiblock and periodic boundaries conditions. For these boundaries, two possibilities arise. The first possibility consists of keeping the interior scheme on boundaries. For periodic boundaries, one obtains a tridiagonal periodic matrix to solve. In case of multiblock multiprocessors computations, this option requires to solve the tridiagonal (even periodic) system in parallel, which may be very expensive. The second possibility is to use ghost cells and degenerate the scheme either by upwinding or by decreasing the order of accuracy. This is generally done by using a boundary scheme one order lower than the interior boundary scheme based on the works of Gustafsson [8], who shows that for hyperbolic problems, using explicit FD schemes, this insures the global scheme to keep the order of accuracy of the interior. But Kobayashi [12] shows, for Padé-like FV scheme, that the order of accuracy for the global scheme reduce to the one of the boundary closure. Therefore, decreasing the order of accuracy of the scheme could reduce the accuracy order on the whole domain. However, as important is to preserve high precision, another important constraint is to keep the conservativeness of the FV scheme and the stability.

In this work, only schemes using two ghost cells are investigated (see Fig. 6).

2.5.1. Centered explicit boundary scheme (CEBC)

The first scheme consists of using an explicit fourth-order interpolation on the first interface 1/2:

$$\tilde{u}_{1/2} = a\bar{u}_{-1} + b\bar{u}_0 + c\bar{u}_1 + d\bar{u}_2. \tag{20}$$

Then all other interfaces are computed with the usual sixth-order scheme. The stability analysis of the space discretization operator has shown that the scheme is stable on uniform meshes (see Fig. 7). The spectral resolution has been studied for all frequencies on an uniform mesh with 40 cells. Fig. 8(a) shows that the scheme has good spectral resolution on the two first cells on each side of the domain but it presents possibility of anti-diffusion at the two last points of the domain for middle frequencies. However numerical tests have highlighted that the scheme become unstable on mesh with a stretching at the boundary even if the growth of the mesh size is only about 5% (see Fig. 7). To fix these problems, two other possibilities have been explored.

2.5.2. Upwind compact boundary scheme (UCBC)

It is proposed to use a decentered fourth-order compact scheme at the boundary as:

$$\tilde{u}_{1/2} + \alpha\tilde{u}_{3/2} = a\bar{u}_{-1} + b\bar{u}_0 + c\bar{u}_1 + d\bar{u}_2. \tag{21}$$

To obtain the scheme on the last interface, the stencil is just reversed.

The scheme is clearly non-conservative, since the value at interface between two blocks is computed differently on the two blocks. This latter point is a disadvantage which could be corrected by applying a Riemann solver (e.g. Roe solver) with the two values computed on each block. For example let Σ be an interface between Blocks 1 and 2 as illustrated in Fig. 9. A left value $\tilde{u}^1_{N^1+1/2}$ on Σ is computed using the decentered compact scheme on Block 1, and the right value $\tilde{u}^2_{1/2}$ is computed on Block 2. Then, the flux on Σ is obtained thanks to the Roe solver:

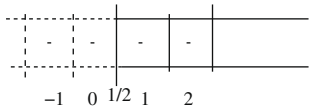

Fig. 6. Ghost cells on the left boundary of the domain: cells indexed-1 and 0 are ghost cells, the interface 1/2 is the boundary interface of the domain.

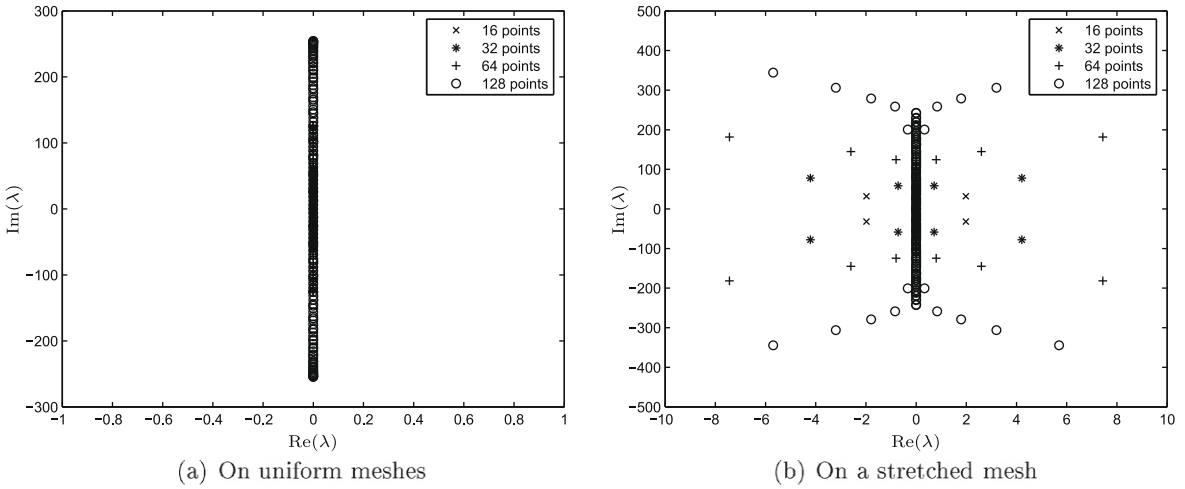

Fig. 7. Eigenvalues spectra of the whole scheme using the centered explicit boundary scheme (CEBC) on meshes of 16, 32, 64 and 128 points.

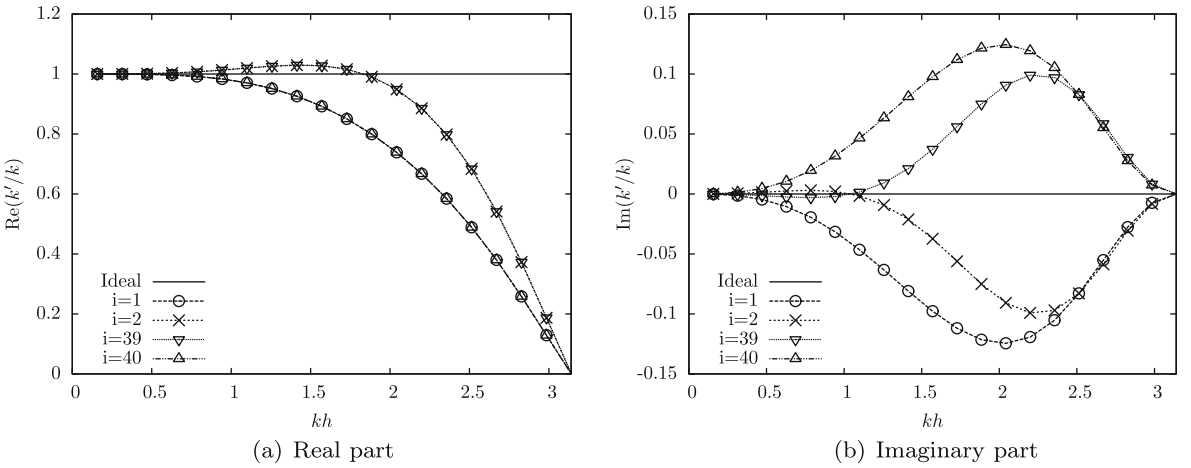

Fig. 8. k'/k for the first derivatives in cells at boundaries using the centered explicit boundary scheme (CEBC).

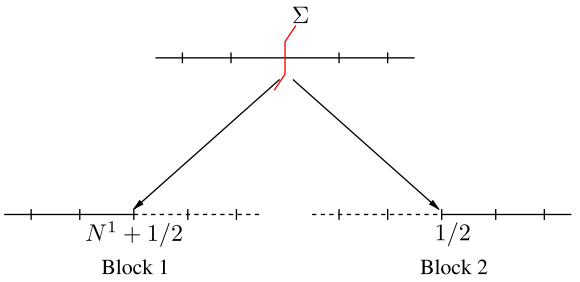

Fig. 9. Roe correction for a decentered scheme on a boundary.

$$F_\Sigma = F^1_{N^1+1/2} = F^2_{1/2} = F_{\text{Roe}}(\tilde{u}^1_{N^1+1/2}, \tilde{u}^2_{1/2}).$$

This Roe solver allows to account for the wave propagation direction. It does not correct anti-diffusion at near boundary cells (see Fig. 11(a) and (b)) but the eigenvalues study reveals that the scheme remains globally stable even on stretched meshes (see Fig. 10(a) and (b)) for $-1 \leqslant \alpha < 1$. Unfortunately, this approach is too expensive in parallel communications.

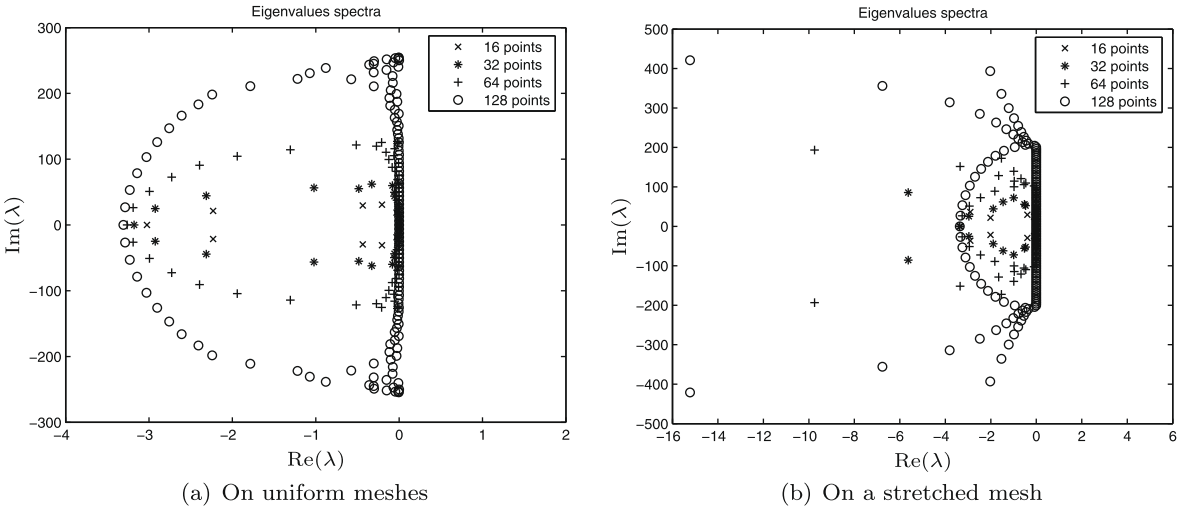

Fig. 10. Eigenvalues spectra of the whole scheme using the UCBC ($\alpha = 2/3$) with a Roe solver boundary scheme on meshes of 16, 32, 64 and 128 points.

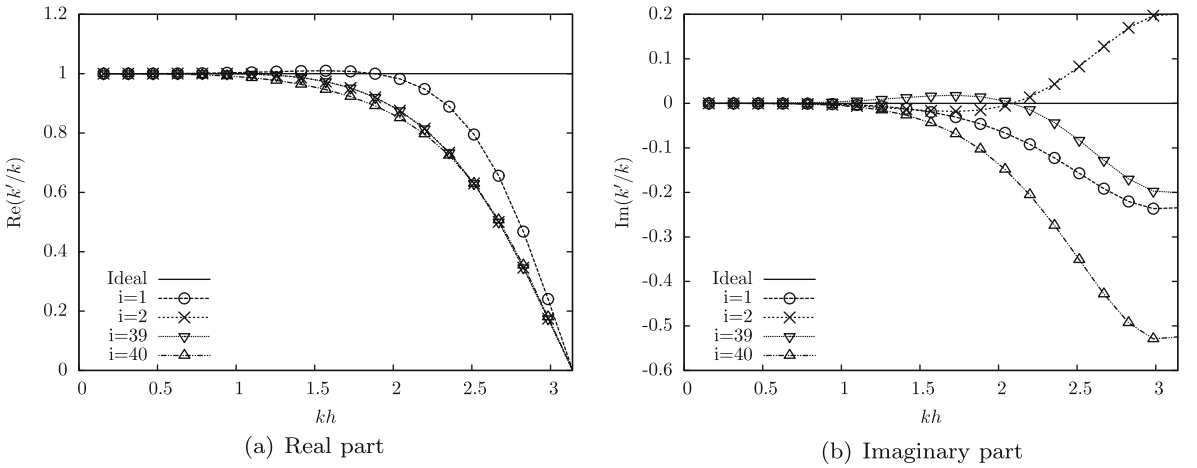

Fig. 11. k'/k for the first derivatives in cells at boundaries using the UCBC ($\alpha = 2/3$) with a Roe solver boundary scheme.

2.5.3. Decentered compact near boundary scheme (DCNBC)

This third approach aims to be a mix of the two previous methods. Here, the explicit fourth-order scheme is used on the first interface (1/2), while a decentered fifth-order compact scheme is employed on the second interface (3/2). To obtain a fifth-order scheme, only interior cells are used:

$$\alpha\tilde{u}_{1/2} + \tilde{u}_{3/2} + \beta\tilde{u}_{5/2} = b\bar{u}_1 + c\bar{u}_2 + d\bar{u}_3. \tag{22}$$

This boundary closure is globally stable on uniform grids (see Fig. 12). Although some eigenvalues have positive real part on stretched grids (Fig. 12(b)), numerical tests have shown that it is more stable than the CEBC. The whole scheme also presents possibility of anti-diffusion at middle and high frequencies on boundaries (Fig. 13). Anti-diffusion at middle frequencies is less severe than on CEBC scheme. Anti-diffusion on high frequencies can be eliminated by filtering. Actually, filtering is generally needed to eliminate these high frequencies which are not solved by the scheme.

2.5.4. Summary

The three proposed boundary schemes have shown the same behaviour in terms of dispersion (real part of k'), which is present just at high frequencies; but for CUBC, this appears for higher frequencies than for CEBC or DCNBC.

In terms of anti-diffusion, the CEBC scheme generates such phenomena even for middle frequencies while it is less severe for DCNBC and inexistant for CUBC. This amplification appears at higher frequencies for the two last schemes, especially for CUBC. However this behaviour is not so dramatic since special numerical treatment could be applied to damp these spurious waves. Even if CUBC seems to perform better, it will not be implemented in our solver for computational cost reasons.

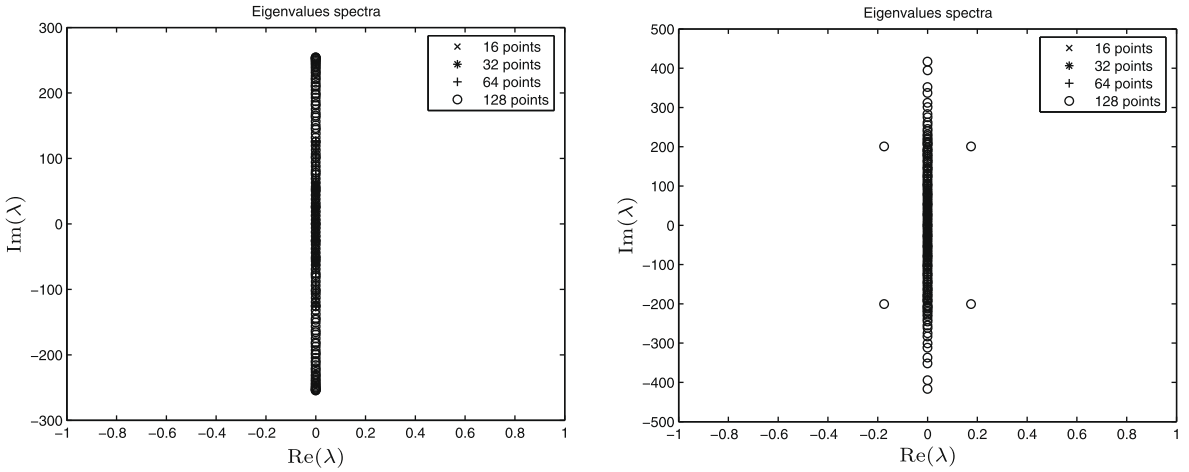

(a) On uniform meshes (b) On a stretched mesh

Fig. 12. Eigenvalues spectra of the whole scheme using the DCNBC on meshes of 16, 32, 64 and 128 points.

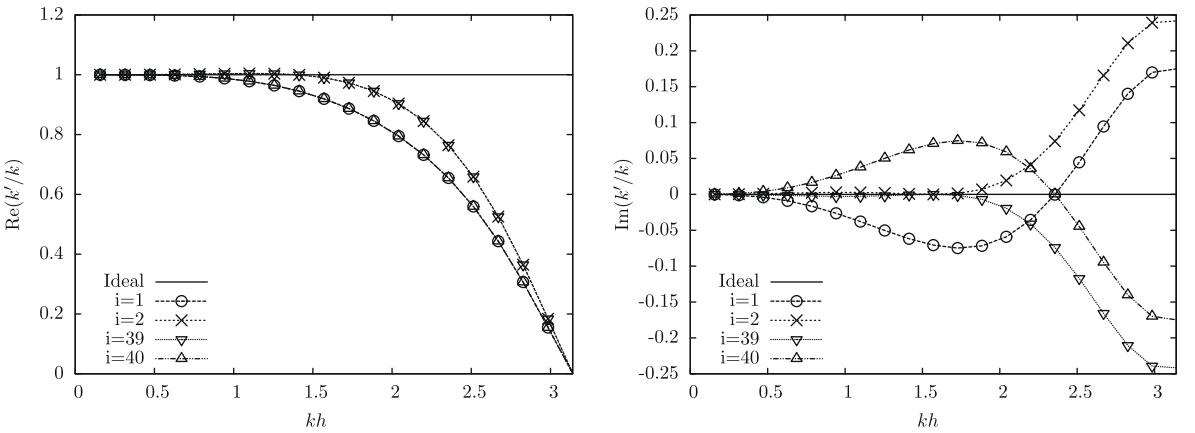

(a) Real part (b) Imaginary part

Fig. 13. k'/k for the first derivatives in cells at boundaries using DCNBC.

3. Extension to non-linear cases

3.1. Discretization of the compressible Euler equations

Here are considered the compressible Euler equations written in conservative form:

$$\frac{\partial W}{\partial t}+\frac{\partial E}{\partial x}+\frac{\partial F}{\partial y}+\frac{\partial G}{\partial z}=0, \tag{23}$$

where

$$W=(\rho,\rho u,\rho v,\rho w,\rho e)^t, \tag{24}$$

is the vector of conservative variables and

$$E=\left(\rho u,\rho u^2+p,\rho uv,\rho uw,(\rho e+p)u\right)^t,$$
$$F=\left(\rho v,\rho uv,\rho v^2+p,\rho vw,(\rho e+p)v\right)^t,$$
$$G=\left(\rho w,\rho uw,\rho vw,\rho w^2+p,(\rho e+p)w\right)^t$$

are the convective flux densities.

The FV formulation requires to approximate the fluxes defined by

$$\tilde{\mathcal{F}}_{i+1/2,j,k} = \int_{S_{i+1/2,j,k}} (En_x + Fn_y + Gn_z)\mathrm{d}\sigma, \tag{25}$$

on the interface $(i+1/2, j, k)$. If assumed that the normal is constant along the interface, this leads to find an approximation of:

$$\tilde{\mathcal{F}}_{i+1/2,j,k} = S(\widetilde{E}\tilde{n}_x + \widetilde{F}\tilde{n}_y + \widetilde{G}\tilde{n}_z), \tag{26}$$

where $\widetilde{E}$, $\widetilde{F}$ and $\widetilde{G}$ are interface-averaged values of fluxes, and $(\tilde{n}_x, \tilde{n}_y, \tilde{n}_z)$ is the unitary normal of the interface.

To obtain a high-order compact FV scheme based on the compact interpolations presented in the previous sections, different approaches could be followed [17,18,13,19]. One of these approaches is to approximate $\widetilde{E}$, $\widetilde{F}$ and $\widetilde{G}$ using interface-averaged values of conservative or primitive fields computed using the compact interpolation. However, when computing fluxes using interpolated mean values, a problem of precision arises. For instance, it is needed to compute the mean of the product ρu, $\langle \rho u \rangle$, to approximate the flux. But approximating $\langle \rho u \rangle$ by $\langle \rho \rangle \langle u \rangle$ is a second-order approximation. An idea is then to compare the two values in order to determine which correction could be done to keep a higher order. Pereira et al. [17] shows that it is possible to make a correction to obtain a fourth-order approximation at a reasonable cost. This requires to approximate the first- and second-order derivatives respectively at the second- and first-order for ρ and u. This correction, extended by Lacor et al. [13] to arbitrary schemes notably improved the precision of his scheme on a rotation of a Gaussian wave test case. However, the correction was done assuming a cartesian grid since for a general grid highly there is an important increase the cost of the computations. For sake of convenience, this approach and the others will be discussed in details in a next paper with more appropriate test cases since in the applications presented in the present paper, they do not make a valuable difference.

Therefore, for the vortex convection and acoustic scattering problems handled in the present paper, the following MUSCL-like formulation (which is formally of the second-order) is used, for each interface $(i+1/2, j, k)$:

$$\tilde{\mathcal{F}} \approx S(E(\widetilde{W})\tilde{n}_x + F(\widetilde{W})\tilde{n}_y + G(\widetilde{W})\tilde{n}_z), \tag{27}$$

where, $\widetilde{W}$ is the vector of the $(i+1/2, j, k)$ interface-averaged values of the conservative variables.

3.2. Slip wall boundary condition treatment

In order to address some acoustic test cases, it is necessary to discuss the implementation of the slip wall boundary condition. This condition is treated as a symmetry condition. In the same way as multiblock and periodic boundary conditions it involves two layers of ghost cells whose metrics (points, normals, kinetic moments) and conservative fields are defined by symmetry. Indeed, let Σ in Fig. 14 be a symmetric boundary. Let M' be the symmetric of the point M with respect to Σ, following the normal $\mathbf{n}$. The symmetry condition induces:

$$\begin{cases} \rho(M') = \rho(M), \\ \mathbf{u}(M') = \mathbf{u}(M) - 2(\mathbf{u}(M).\mathbf{n})\mathbf{n}, \\ p(M') = p(M). \end{cases} \tag{28}$$

It is then possible to use on this boundary either the CEBC or the DCNBC closures. For all test cases, the DCNBC closure has been applied.

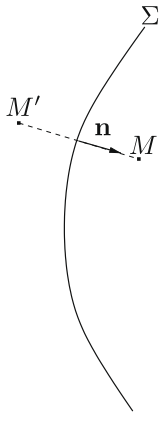

Fig. 14. Symmetric boundary condition.

4. Numerical stabilization

All spectral studies have shown that there is possibility of anti-diffusion of the scheme at high frequencies near boundaries. Thus, computations need to be stabilized. Filtering is a possible way to achieve it. The filters chosen are compact filters, precisely the sixth-order and eight-order filters proposed by Gaitonde and Visbal [4] have been used. The inner filter scheme reads:

$$\alpha_f \hat{u}_{i-1} + \hat{u}_i + \alpha_f \hat{u}_{i+1} = \sum_{n=-N}^{N} a_n \bar{u}_{i+n}, \tag{29}$$

where α_f is a parameter ranging from $-1/2$ to $1/2$. The authors also recommend to use higher order one-sided formulas on boundaries instead of decreasing the order of the filter. The one-sided formulas are defined by

$$\hat{u}_1 = \bar{u}_1, \tag{30}$$

$$\alpha_f \hat{u}_{i-1} + \hat{u}_i + \alpha_f \hat{u}_{i+1} = \sum_{n=1}^{2N+1} a_n \bar{u}_n, \quad i = 2, \ldots, N. \tag{31}$$

The filtering is applied in the computational plane. In multidimensional case, filtering operator is applied successively in each dimension. One can remark that, in each direction, the first and the last points are not filtered. This could be a drawback since anti-diffusion is possible at this point. But for multiblock and periodic problems, it is possible to avoid it by using the two ghost cells values, so the first point non-filtered is fictitious.

5. Applications

In this section, linear and non-linear test cases are performed. The results of the proposed schemes are compared with two schemes using constant coefficients for the interface-averaged value interpolation. The first one (CEN4) is obtained using the explicit centered interpolation with constant coefficients, fourth-order on uniform grids, defined by

$$\tilde{u}_{i+1/2} = -\frac{1}{12}\bar{u}_{i-1} + \frac{7}{12}\bar{u}_i + \frac{7}{12}\bar{u}_{i+1} - \frac{1}{12}\bar{u}_{i+2}. \tag{32}$$

The second one (COMP46) is obtained using the compact interpolation with constant coefficients, sixth-order on uniform grids, defined by Eq. (9) for interior interfaces and the above explicit fourth-order centered interpolation equation (32) on the periodic boundary interfaces.

The first part of this section presents a model problem of linear convection on different types of grids. Then follows the presentation of some non-linear applications.

5.1. Linear convection

In order to numerically assess the effective numerical properties of the schemes studied, a 2D linear convection problem is considered:

$$\frac{\partial \phi}{\partial t} + \mathbf{v}.\nabla\phi = 0. \tag{33}$$

An initial Gaussian wave

$$\phi(x,y) = 1 + 0.25\exp(-38.(x^2 + y^2)),$$

is convected through a computational domain comprised in the square region $-1 \leqslant x,\ y \leqslant 1$ at the speed $\mathbf{v} = (1,1)$. Periodic boundary conditions are applied on all boundaries. The convection following this diagonal direction makes the test case really sensitive to boundary closures and breaks the preferred direction which could exists in the used grids.

The time integration scheme used for these computations is the following four steps Runge–Kutta method [11]

$$\begin{cases} u^{(0)} = u_n, \\ u^{(k)} = u^{(0)} + \alpha_k \Delta t L(u^{(k-1)}), \quad k = 1, \ldots, 4, \\ u_{n+1} = u^{(4)}, \end{cases} \tag{34}$$

with L, the space discretization operator and

$$\alpha_1 = \frac{1}{4}, \quad \alpha_2 = \frac{1}{3}, \quad \alpha_3 = \frac{1}{2}, \quad \alpha_4 = 1.$$

This scheme is fourth-order accurate for linear problems.

In summary, four numerical schemes have been numerically studied:

1. CART46 which uses the cartesian-like sixth-order compact scheme using curvilinear abscissa for the interior interfaces and the CEBC closure scheme.
2. CART456 which differs from the previous in that it uses the DCNBC closure scheme.

3. CUR46 which is the general FV curvilinear scheme using the CEBC closure scheme.
4. CUR456 which is the general FV curvilinear scheme using the DCNBC closure scheme.

It is worth reminding that on cartesian uniform grids, the CART46, CUR46 and COMP46 schemes are the same. On another hand, the CART456 and the CUR456 schemes are the same.

Concerning the CURxxx methods, two types of parameters are to be specified: the local reference frame and the weights used for the least square method. The codes (ORTH, NORM and GEN) of the local reference frames used are shown in Table 3. The combinations of weights (W1, W2 and W3) used described in Table 4. When it is not specified, the local reference frame ORTH and the weights combination W2 is used.

The different schemes are often coupled with the filter operator. When it is the case, it is mentioned in the title of the scheme using the letter F followed by the order of the filter and the coefficient of the filter (e.g.: F80.49 for the eight-order filter with $\alpha_f = 0.49$). The filter is applied after the last Runge–Kutta step.

Different meshes are used in order to highlight different properties of the proposed schemes. Therefore, to retrieve the numerical order of the schemes, only meshes which can be refined or coarsened using the same initial property of the mesh are used: uniform cartesian and wavy meshes. All meshes help to assess the stability, the dissipation and dispersion properties of the schemes. Stretched cartesian grid and non-uniform cartesian grid consisting in alternating bigger and smaller cells help to assess the importance of taking into account non-uniformity on cartesian grid. On another hand, wavy grids and highly irregular grid obtained by randomly perturbing an uniform cartesian grid highlight the importance of taking into account shape, size and direction variations in curvilinear grids.

Hence, seven types of grids have been used (see Figs. 15 and 16):

- UNIF: uniform cartesian grid.
- STRETCH: a stretched cartesian grid with a maximum stretch ratio of 1.05.
- ALT: a cartesian grid consisting in alternating bigger and smaller cells with a size ratio of 11/9.
- WAVY I: an uniform wavy grid defined by

Table 3
Codes of the local reference frames used for the CURxxx methods.

Code	Local reference frame
ORTH	Orthonormal local reference frame with the x' direction defined by the direction between the adjacent cells centers (Fig. 3(a))
NORM	Orthonormal local reference frame with the x' direction defined by the normal of the face (Fig. 3(b))
GEN	Non-orthogonal local reference frame with the direction defined by the neighbouring cells centers (Fig. 3(c))

Table 4
Weights used in general for the least square method applied on transverse derivatives relations: the z' derivatives are not considered in 2D cases.

Derivatives	Weights W1	Weights W2	Weights W3
1st order: $\partial y', \partial z'$	1	100	500
2nd order: $\partial^2 x'y',\ \partial^2 y'^2,\ \partial^2 x'z', \ldots$	1	100	500
3nd order: $\partial^3 x'y'^2,\ \partial^3 x'z'^2,\ \partial^3 x'^2 y', \ldots$	1	1	1

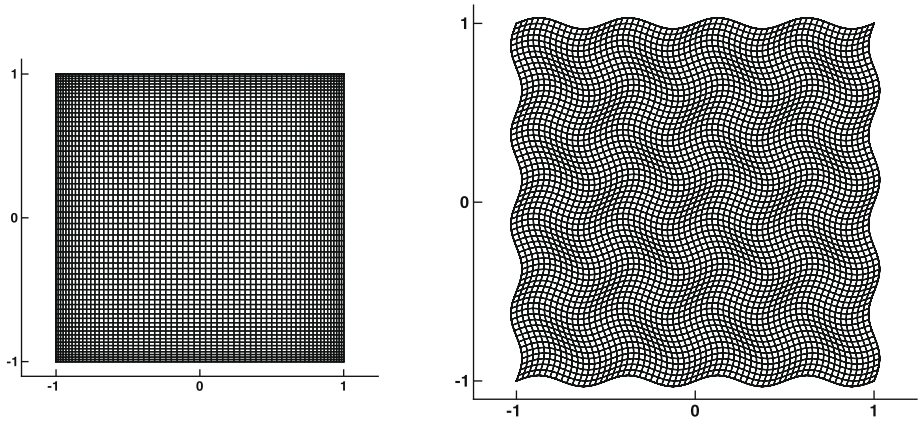

(a) Stretched cartesian mesh (STRETCH) (b) Uniform wavy mesh (WAVY I)

Fig. 15. 64 × 64-cells meshes used for computations.

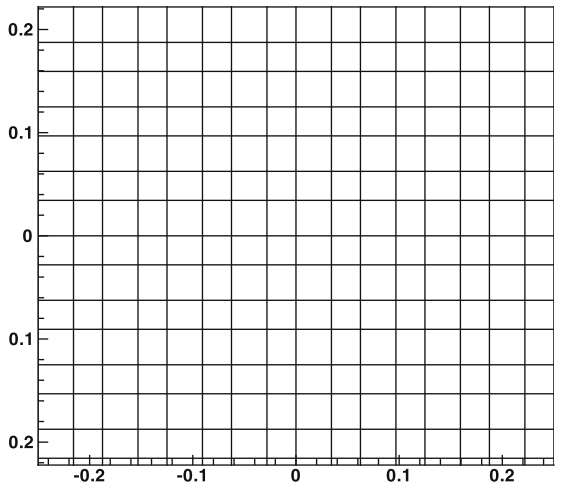

(a) Cartesian grid alternating bigger and smaller cells with the size ration 11/9 (ALT)

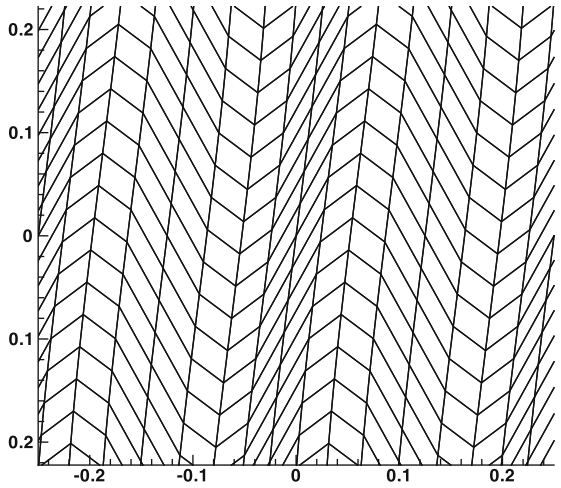

(b) Highly distorded wavy mesh obtained from the UNIF grid (WAVY II)

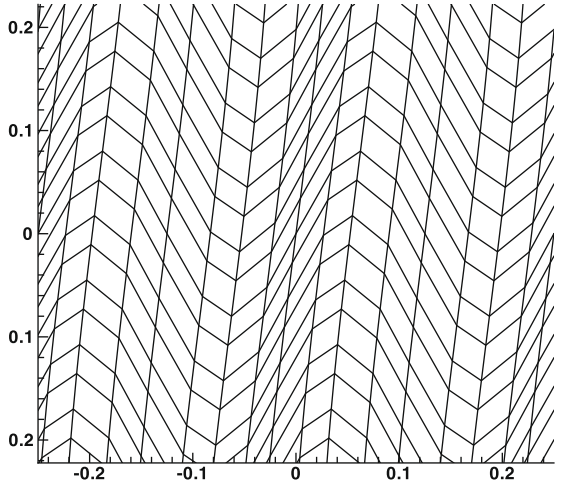

(c) Highly distorded wavy mesh obtained from the ALT grid (WAVY III)

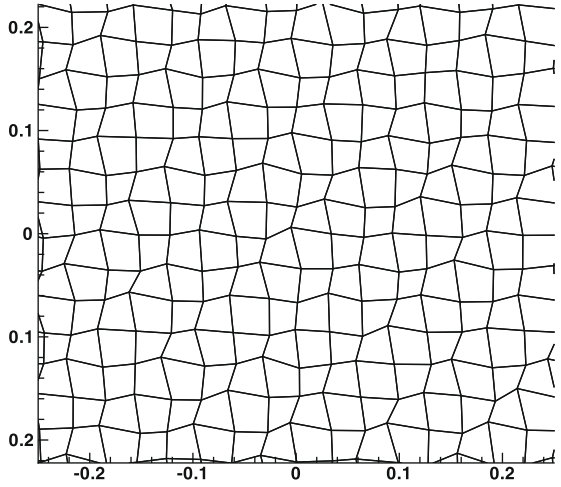

(d) Perturbed mesh obtained by randomly perturbing the UNIF grid (RAND)

Fig. 16. 64 × 64-cells ALT, WAVY II, WAVY III and RAND meshes magnified.

$$\begin{cases} x_{ij} = x_{\min} + \Delta x\left[(i-1) + A_x \sin\left(\frac{n_x \pi (j-1)\Delta y}{L_y}\right)\right] \\ y_{ij} = y_{\min} + \Delta y\left[(j-1) + A_y \sin\left(\frac{n_y \pi (i-1)\Delta x}{L_x}\right)\right] \end{cases}, \tag{35}$$

with

$$1 \leqslant i, \quad j \leqslant N$$

$$\Delta x = \frac{L_x}{N-1}, \quad \Delta y = \frac{L_y}{N-1},$$

where N denotes the number of points in the x and y directions, $L_x = x_{\max} - x_{\min}$ and $L_y = y_{\max} - y_{\min}$ are the lengths of the domain in the x and y directions respectively. $n_x = n_y = 8$ and $A_x = A_y = 2/r$ where r is fixed such that $rN = 128$. This parameter r allows to obtain a mesh which is a coarsen mesh of the mesh obtained with $N = 128$ and $r = 1$.

- WAVY II: a highly distorded uniform wavy grid defined by

$$\begin{cases} x_{ij} = \bar{x}_{ij} + 0.02 L_x \sin\left(2\pi \frac{(\bar{y}_{ij} - y_0)}{L_y}\right) \\ y_{ij} = \bar{y}_{ij} + 0.04 L_y \sin\left(16\pi \frac{(\bar{x}_{ij} - x_0)}{L_x}\right) \end{cases}, \tag{36}$$

where $(\bar{x}_{ij}, \bar{y}_{ij})$ are the coordinates of the cartesian uniform mesh of the same size, L_x and L_y, the lengths of the domain in the x and y directions respectively, and (x_0, y_0), the center of the domain.

- WAVY III: a highly distorded wavy grid obtained from the ALT grid of the same size using Eq. (36);
- RAND: a highly irregular grid obtained by randomly perturbing an uniform grid with a maximum amplitude of 20%.

5.1.1. Effective order of accuracy

To measure the numerical order of accuracy of the different schemes, the three types of grids used are the UNIF, WAVY I and WAVY II grids. For the first two types, four different grid resolutions have been considered to retrieve the effective order of accuracy: 16×16, 32×32, 64×64 and 128×128. For the WAVY II grids, a 256×256 grid is also used since the 16×16 grid is so coarse that the domain defined by WAVY II grids is not well described.

The time step is chosen very small so that the time integration error could be neglected in comparison to the spatial one. The error between the computed solution after one period (*i.e.* the time for the wave to return to the initial position for the first time) and the initial solution is found using the L_2-norm. Fig. 17 displays the evolution of the error versus the mesh size and Tables 5–7 give the observed order of accuracy obtained on the uniform cartesian and wavy grids. For sake of clarity, for WAVY I and WAVY II grids, only the errors for CART46, CUR46 and COMP46 schemes are plotted on graphs.

On the more distorded wavy mesh (WAVY II), CARTxxx and CURxxx methods need to be stabilized with filtering. And when filtered, the errors obtained are almost the same for CART46 and CART456 schemes and for CUR46 and CUR456 schemes. It is noteworthy that the NORM frame is used since it was impossible to stabilize computations using the ORTH frame for this WAVY II mesh. This is explained further when dealing with long-time convection simulations.

One can see that the averaged order of accuracy of the different methods for UNIF and WAVY I grids is higher than 5. The results for the WAVY II grids are more difficult to explain. In fact, the order retrieved when passing from the 16×16 grid to the 32×32 grid is less than one. The reason has already been mentioned: the 16×16 grid is too coarse to well discretize the domain defined by other WAVY II grids, and therefore this grid is probably out of the asymptotic range. This grid is almost

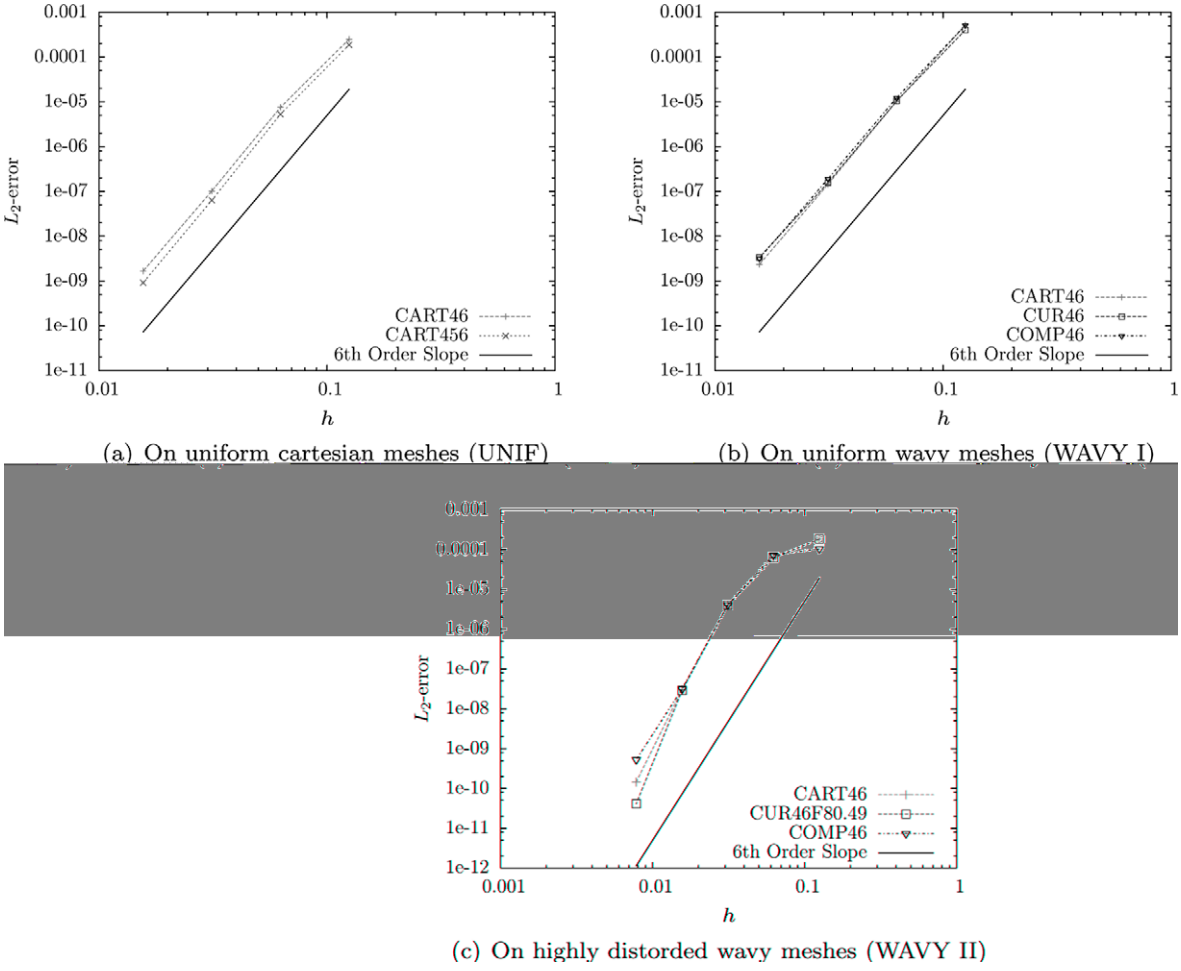

Fig. 17. Evolution of the errors following the mesh size for the 2D linear convection.

Table 5
Numerical mean errors and orders of schemes on uniform cartesian meshes (UNIF) for the 2D linear convection.

Mesh size	CART46		CART456	
	Error	Order	Error	Order
16×16	2.52×10^{-4}	–	1.88×10^{-4}	–
32×32	7.55×10^{-6}	5.06	5.31×10^{-6}	5.14
64×64	1.02×10^{-7}	6.20	6.36×10^{-8}	6.38
128×128	1.67×10^{-9}	5.93	9.16×10^{-10}	6.11

Table 6
Numerical mean errors and orders of schemes on uniform wavy meshes (WAVY I) for the 2D linear convection.

Mesh size	CART46		CUR46		COMP46	
	Error	Order	Error	Order	Error	Order
16×16	5.13×10^{-4}	–	4.01×10^{-4}	–	5.13×10^{-4}	–
32×32	1.03×10^{-5}	5.63	1.05×10^{-5}	5.25	1.23×10^{-5}	5.38
64×64	1.44×10^{-7}	6.16	1.57×10^{-7}	6.06	1.91×10^{-7}	6.00
128×128	2.34×10^{-9}	5.94	3.36×10^{-9}	5.54	3.18×10^{-9}	5.9

	CART456		CUR456	
	Error	Order	Error	Order
16×16	5.33×10^{-4}	–	3.91×10^{-4}	–
32×32	7.56×10^{-6}	6.13	7.72×10^{-6}	5.66
64×64	8.68×10^{-8}	6.44	1.00×10^{-7}	6.27
128×128	1.31×10^{-9}	6.05	2.85×10^{-9}	5.13

Table 7
Numerical mean errors and orders of schemes on highly distorded wavy meshes (WAVY II) for the 2D linear convection.

Mesh size	CART46F80.49		CUR46F80.49-NORM		COMP46	
	Error	Order	Error	Order	Error	Order
16×16	1.84×10^{-4}	–	1.84×10^{-4}	–	1.04×10^{-4}	–
32×32	6.23×10^{-5}	1.56	6.22×10^{-5}	1.56	7.35×10^{-5}	0.50
64×64	4.0×10^{-6}	3.96	4.01×10^{-6}	3.95	4.08×10^{-6}	4.17
128×128	3.03×10^{-8}	7.04	2.91×10^{-8}	7.10	3.14×10^{-8}	7.02
256×256	1.46×10^{-10}	7.69	4.12×10^{-11}	9.46	5.29×10^{-10}	5.89

	CART456F80.49		CUR456F80.49-NORM	
	Error	Order	Error	Order
16×16	1.84×10^{-4}	–	1.84×10^{-4}	–
32×32	6.23×10^{-5}	1.56	6.22×10^{-5}	1.56
64×64	4.01×10^{-6}	3.95	4.02×10^{-6}	3.95
128×128	3.04×10^{-8}	7.04	2.94×10^{-8}	7.09
256×256	1.47×10^{-10}	7.68	4.87×10^{-11}	9.23

uniform but with slight deformations in the y direction so the COMP46 method performed very well while the other methods introduces some errors because the filtering was used. When passing from the 128×128 grid to the 256×256 grid, the usage of the scheme in physical space probably allows to cancel out more higher-order terms than formally predicted than the COMP46 method.

5.1.2. Stability, dissipation and dispersion properties on uniform grids

To analyze the stability, the dispersion and dissipation of the different schemes, computations have been carried out for 25 periods on the 64×64 grids. This section presents the results obtained on uniform grids UNIF, WAVY I and WAVY II. It is shown that the proposed schemes behave well on uniform grids. The results obtained on the WAVY II grid highlight the importance of the local reference frame for the CURxxx methods.

Results of the simulation on the uniform grid are shown in Fig. 18. The CEN4 scheme is obviously the most dispersive one since many local extrema are generated. The proposed schemes behaves very well. The eight-order filter does not deteriorate the results obtained.

Fig. 19 shows results obtained on the WAVY I mesh after 25 periods. In this case, COMP46 method is stable and gives good results. It shows that a computational space formulation is stable and efficient on smooth grids even curvilinear. The CART46 and CUR46 methods seems to be the most stable of the proposed schemes since all others need filtering. This shows the

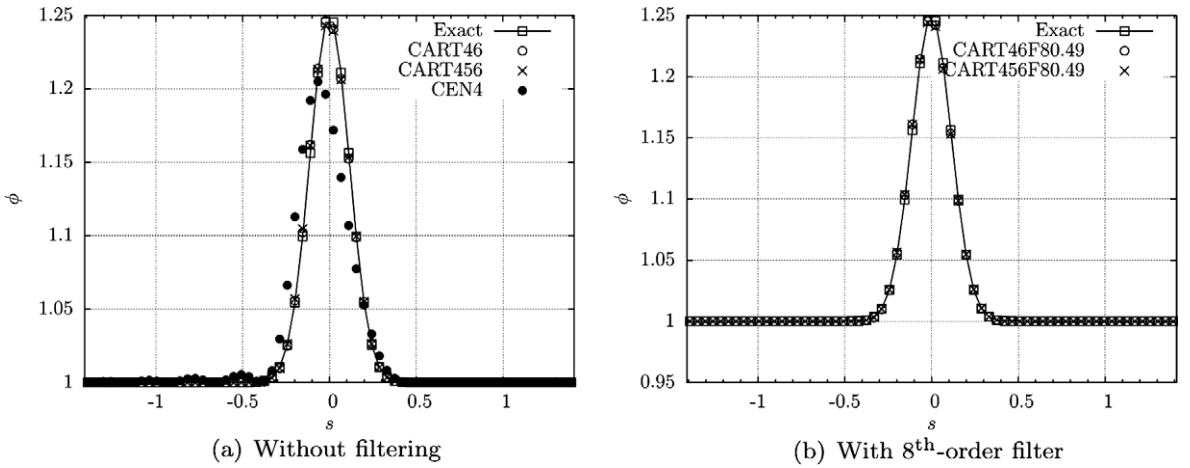

Fig. 18. Profiles along the line $x = y$ of a linear convection equation solution on the uniform cartesian mesh (UNIF) after 25 periods.

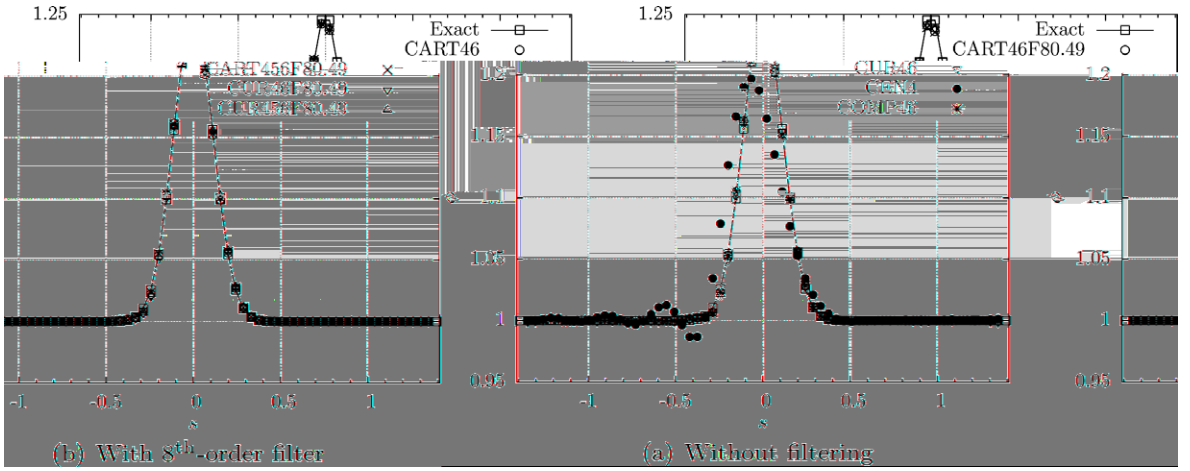

Fig. 19. Profiles along the line $x = y$ of a linear convection equation solution on the uniform wavy mesh (WAVY I) after 25 periods.

limitations of a 1D approach as it has been done in the eigenvalues and spectral study of Section 2.5 to analyze the stability of a scheme on curvilinear grids. Until now, no explanation has been found to justify this phenomenon. However when filtering is applied all the methods give similar results.

It is worth noting that the eighth-order filter with one-sided formulas failed to stabilize CART456 and CUR456 schemes. But the cyclic eight-order filter (not using eight-order one-sided formulas on boundaries), which is used for the results shown, stabilizes the computations. This problem could come either from the one-sided formulations on boundaries either from the fact that the first point is not filtered. Results obtained on the vortex convection and presented further show that the latter fact is probably the main reason. Therefore, it is inadequate to leave the first cell of the domain unfiltered as it is done with one-sided filter on boundaries.

Since, on wavy meshes, filtered CARTxxx methods behave similarly, as well as CURxxx, computations results on the highly distorded mesh (WAVY II) are shown only for schemes using the CEBC boundary closure. For this WAVY II mesh, all the methods (even the CEN4 method) are unstable except the COMP46 one. However its results (not shown) are pretty dispersive. To compare them with equal parameters, the filter has been applied to all methods. In Fig. 20(a), one can observe that on highly distorded meshes, the filtered CARTxxx method are finally more dispersive and more dissipative than the scheme using constant coefficients (COMP46) and filtering. One can conclude that it is not sufficient to use the curvilinear abscissa when mesh line directions vary strongly. This is confirmed by results obtained further on non-uniform curvilinear meshes. The filtered COMP46 method is slightly more dissipative than the filtered CURxxx methods.

It is worth noting that the CUR46 method used has been computed using the GEN frame. In Fig. 20(b), a comparison is made between the results obtained with this latter method and those obtained using the orthogonal local frame defined by the interfaces normals. Results are pretty similar, however it could be observed that the results with GEN frame are better

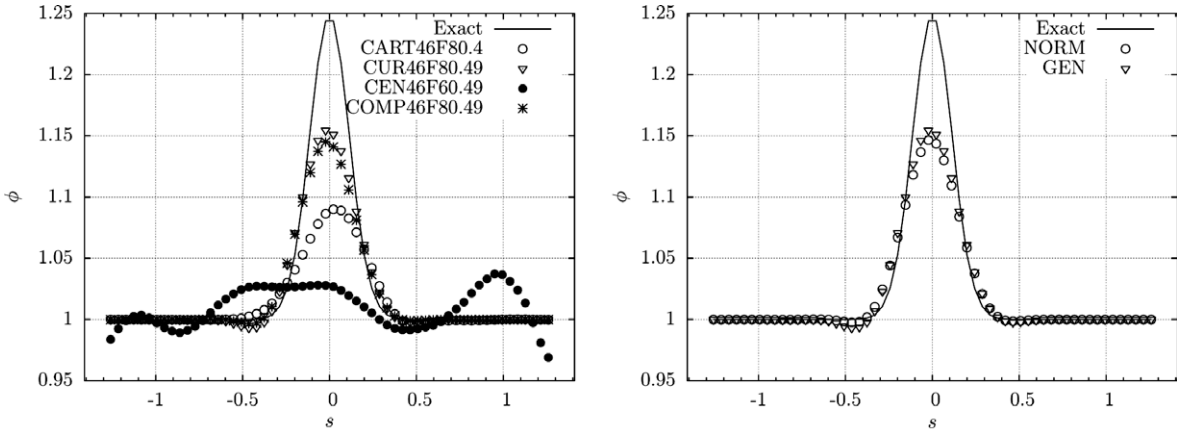

(a) Comparison between the different schemes: CUR46 method is used with the GEN frame

(b) Comparison between the different local frames for the CUR46F80.49-W2 method

Fig. 20. Profiles along the line $x = y$ of a linear convection equation solution on the distorded wavy mesh (WAVY II) after 25 periods.

in terms of dissipation while the NORM ones present a slightly better behaviour in terms of dispersion. The computations using the ORTH frame lead to an non-diagonally dominant matrix to inverse. For these test cases, the restriction to the fourth-order has not been done so the computations are unstable even with the filtering. But this allows to conclude that the local frame plays an effective role (although not sufficient) on the stability and on the dispersion–dissipative effects of the solution. Something noteworthy is the fact that the transverse axe is pretty the same for the NORM and GEN frames. It could indicate that the good discretization of the transverse derivatives in the two frames (as explained in Section 2.2.2) is the reason of the better results obtained. Indeed, this discretization is less good for the CURxxx method with ORTH frame and absent for the CARTxxx methods. On meshes with very strongly varying grid lines directions, the GEN frame is the best to get the lowest dissipation effect.

5.1.3. Stability, dissipation and dispersion properties on nun-uniform cartesian grids

This section presents computations done for 25 periods on 64 times 64 non-uniform cartesian grids STRETCH and ALT. The results obtained on both grids confirms the conclusion of the eigenvalues study of the multiblock boundary closures. Meanwhile the results obtained on the ALT grid highlight the necessity to take into account the non-uniformity of cartesian grids.

Fig. 21 shows results on the stretched mesh after 25 periods. The CART46 method is not stable without filtering whereas the CART456 yields very satisfactory results. Hence, this confirms that on this type of grids, CEBC boundary closure is really less stable than DCNBC boundary closure as foreseen by the eigenvalues study. However, the COMP46 method is stable without filtering. This is easily explained by the fact that, when processing interfaces on the same mesh line, the COMP46 scheme behaves like if the mesh was uniform. Moreover, since the interfaces on this mesh line have the same normal, when

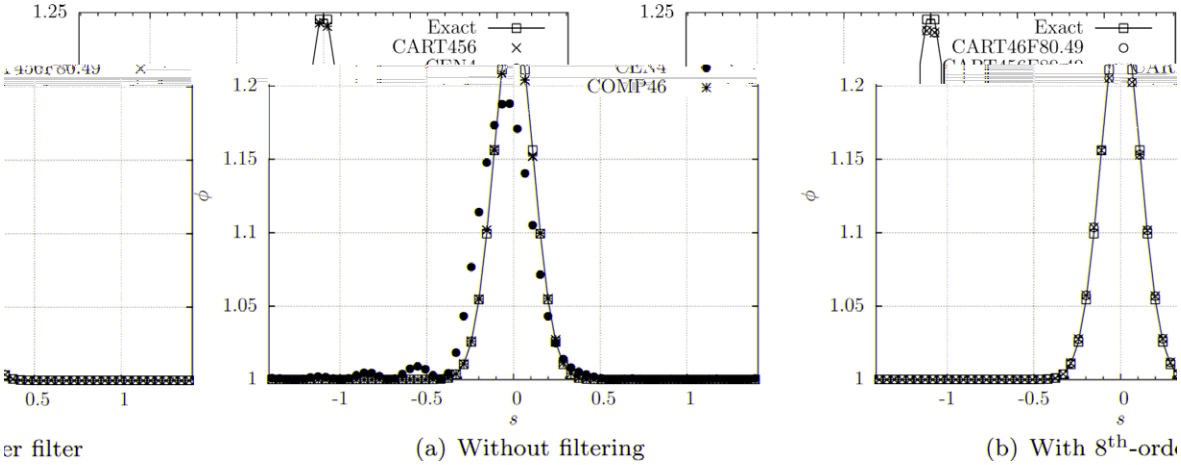

er filter

(a) Without filtering

(b) With 8th-ord

Fig. 21. Profiles along the line $x = y$ of a linear convection equation solution on the stretched cartesian mesh (STRETCH) after 25 periods.

computing the fluxes balances in this mesh line direction, these fluxes balances behave like the 1D space discretization operator on an uniform grid. Therefore the scheme is stable as it is on uniform grids. Taking into account the non-uniformity breaks this stability property for the CART46 scheme.

According to those previous results, it seems like taking into account non-uniformity of the grid is not necessary. Results obtained on the ALT scheme shows that it is certainly not the case. Fig. 22 shows results obtained using the different schemes. Although the COMP46 scheme is stable, it is very dispersive and pretty anti-diffusive. It is therefore possible that the scheme becomes unstable for longer simulations. The poor behaviour of the constant coefficient scheme is surprising since the non-uniformity introduced by the alternating size ratio used is rather small. Once again, the CART46 scheme is not stable while the CART456 one is. The use of the filter does not completely solve the problem. Something interesting to see here is the fact that using the filter introduces little dispersion to the CART456 results, even when using a cyclic formulation. It can indicate that the filter could be also a source of dispersion effects when dealing with non-uniform grids. However, it is clear that taking into account non-uniformity of grids is important.

5.1.4. Stability, dissipation and dispersion properties on non-uniform curvilinear meshes

This section deals with non-uniform curvilinear meshes: RAND and WAVY III. A first interesting conclusion is that, when dealing with non-uniform curvilinear meshes, it is not sufficient and even not recommended to use a scheme using only the curvilinear abscissa. However, it is clearly shown that taking into account shape, size and mesh lines directions variations is important to get lowest dissipation and dispersion effects. Computations done on RAND grid highlight the importance of weights used for the least square method.

The results obtained on the RAND mesh are presented in Fig. 23(a). All schemes are unstable without filtering. Using filtering, CURxxx schemes are obviously superior to CARTxxx and COMP46 schemes in terms of dissipation and dispersion.

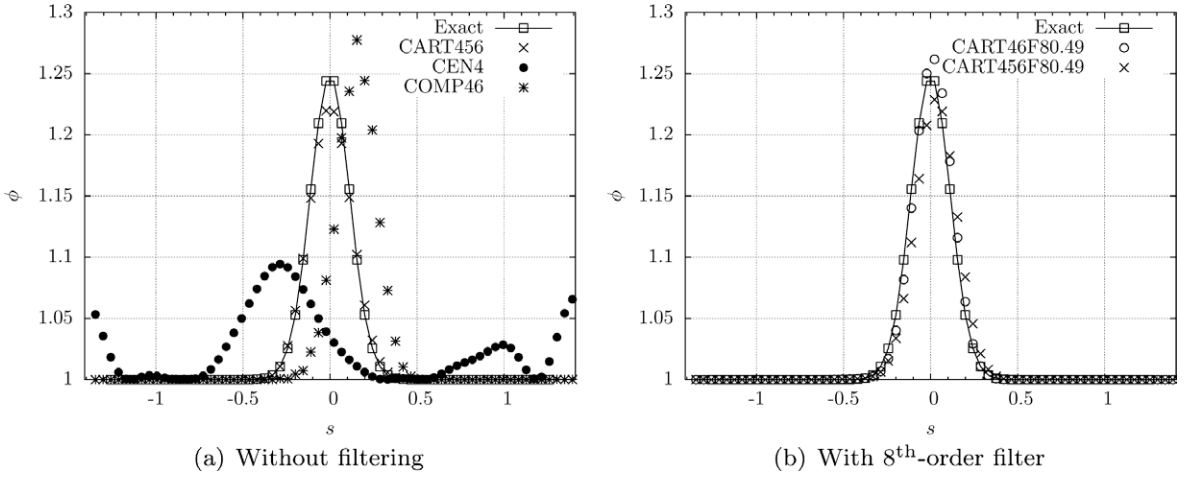

Fig. 22. Profiles along the line $x = y$ of a linear convection equation solution on the mesh alternating bigger and smaller cells with a size ratio of 11/9 (ALT) after 25 periods.

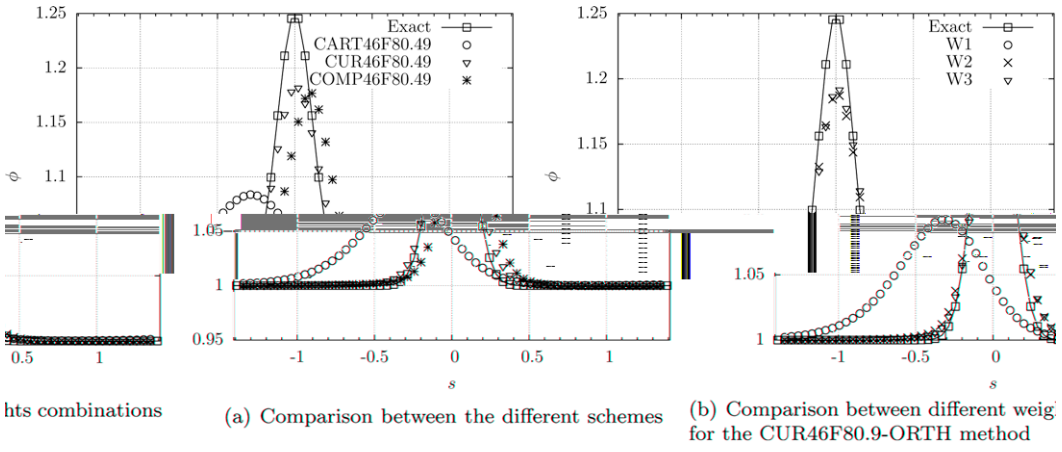

Fig. 23. Profiles along the line $x = y$ of a linear convection equation solution on the RAND mesh after 25 periods.

Dissipation effects are extremely important for CARTxxx schemes. It is possible that those schemes develop strong high frequencies waves which are damped by the filter.

It is important to note that in the weighted least square method, the weight of the first-order and second-order transverse derivatives has to be more important than the higher order transverse derivatives according to results presented in Fig. 23(b). Otherwise CURxxx schemes behave like CARTxxx schemes. The results in Fig. 23(b) also show that the weight combination W2 chosen for all simulations is sufficient to get the best possible results.

Fig. 24 shows results obtained on the WAVY III meshes. None scheme is stable without filtering. Once again, it is clear that CURxxx methods show a better behaviour than all other schemes. Other methods introduce an important dispersion effect which completely denaturates the solution. Thus, the CURxxx methods, which account for the variation of the cells shapes and sizes and of the mesh lines directions, are more capable to handle non-uniform curvilinear meshes.

5.1.5. 3D Computations

To show the capability of the CURxxx schemes to treat three-dimensional flows, a rapid study of the numerical accuracy order and of the stability, dissipation and dispersion properties of the CURxxx scheme have been performed. The same numerical order has been retrieved as it can be seen in Fig. 25.

A long-time convection simulation has been performed but for a larger convection time (50 periods) on a $64 \times 64 \times 64$ RAND mesh. The GEN frame and the W2 weights combination are used. It is noteworthy that, for a limited number of points, the tridiagonal system obtained was not diagonally dominant. In this case, the restriction to the fourth-order by fixing $\alpha = \beta = 1/3$ has been activated. However, the good behaviour of the CURxxx appears clearly in Fig. 26.

5.1.6. Conclusion on linear computations

These numerical tests have shown that the proposed schemes have good accuracy and spectral resolution on regular curvilinear meshes although the more general FV schemes (CURxxx) need to be stabilized for long computations. However,

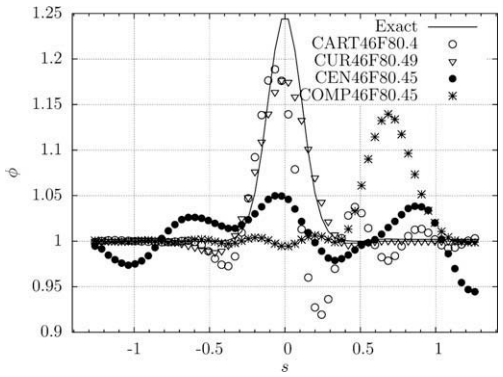

Fig. 24. Profiles along the line $x = y$ of a linear convection equation solution on the WAVY III mesh after 25 periods: the CUR46 method uses the NORM frame.

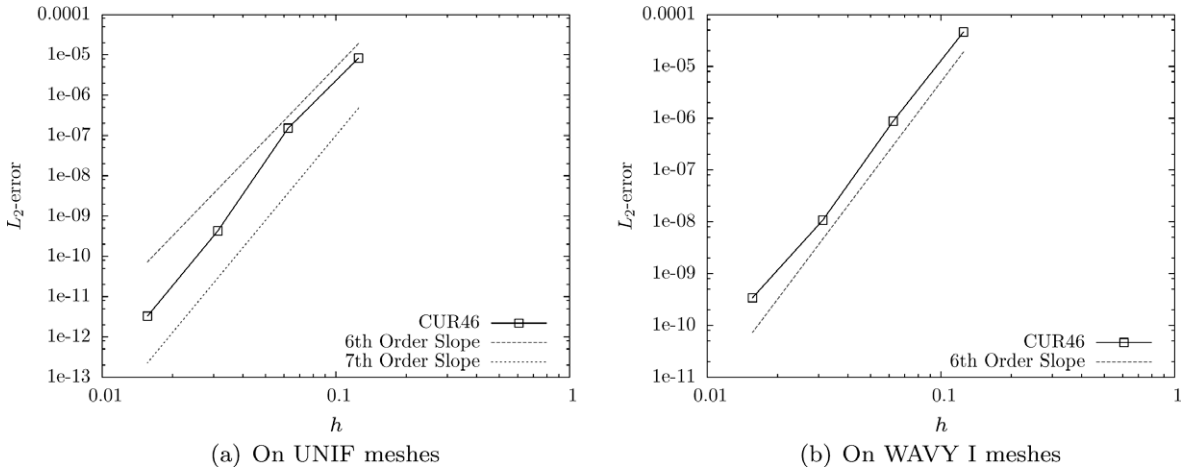

Fig. 25. Evolution of the errors following the mesh size for the 3D linear convection: the GEN Frame and the W2 weights extended to 3D have been used.

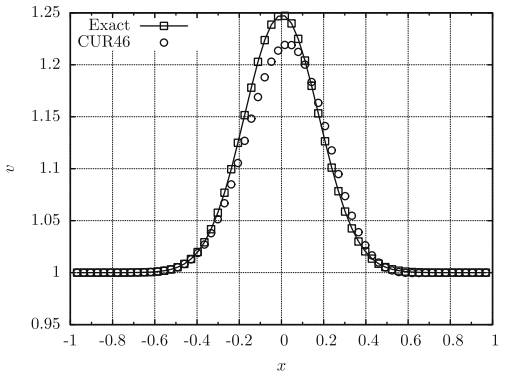

Fig. 26. $y = 0$ profile of a linear convection equation solution on a 3D RAND mesh after 50 periods: the GEN Frame and the W2 weights extended to 3D have been used.

if all methods give pretty similar results on regular meshes, CURxxx schemes are more accurate, low dissipative and low dispersive than the cartesian-like schemes (CARTxxx) and than the schemes using constant coefficients (COMP46) when dealing with irregular curvilinear meshes.

The next sections aim to validate the different schemes with the approach defined by Eq. (27) in a non-linear context and on problems requiring high precision and spectral resolution, some applications have been performed with the code **elsA** of ONERA for aerodynamics simulations [2]. Two test cases have been selected:

- the convection of a vortex on a 2D square region with periodic boundary conditions in all directions;
- the scattering of an acoustic wave diffracted by a plane wall boundary.

All these cases are realized using the following third-order three steps TVD Runge–Kutta algorithm of Gaitonde and Chi-Shu [7]:

$$\begin{cases} u^{(0)} = u_n, \\ u^{(k)} = (1-\alpha_k)u^{(0)} + \alpha_k u^{(k-1)} + \alpha_k \Delta t L(u^{(k-1)}), \quad k = 1,\ldots,3, \\ u_{n+1} = u^{(3)}, \end{cases} \tag{37}$$

with

$$\alpha_1 = 1, \quad \alpha_2 = \frac{1}{4}, \quad \alpha_3 = \frac{2}{3}.$$

Filters have been implemented using one-sided boundaries formulas. However, filters are applied on fictitious cells also so that the unfiltered points are the fictitious cells. So the first points of the domain are filtered and computations are better stabilized. Because of programming constraints, cyclic formulations are not implemented.

5.2. Vortex convection

This numerical test consists of convecting a Lamb–Oseen vortex. The initial vortex is given by the stream function:

$$\Psi(x,y) = \Gamma \exp\left(-\frac{x^2+y^2}{2R^2}\right), \tag{38}$$

where Γ is the vortex strength and R controls the size of the vortex. The resulting velocity distribution is obtained through the velocity stream function relationship:

$$u = U_\infty - \frac{\partial \Psi}{\partial y}, \quad v = V_\infty + \frac{\partial \Psi}{\partial x}. \tag{39}$$

Γ is chosen small (0.004) so that the speed of the vortex is much lower than the mean flow speed to test the resolution of the schemes. R is set equal to 0.15. The associated pressure variation follows the radial momentum equation:

$$p - p_\infty = -\frac{\rho \Gamma^2}{2R^2} \exp\left(-\frac{x^2+y^2}{R^2}\right). \tag{40}$$

The convection will be done on the domain $-1 \leqslant x,\ y \leqslant 1$ at the speed $\mathbf{v}_\infty = (U_\infty, V_\infty) = (1,1)$. The four boundaries are defined as periodic. In this case also, the convection following diagonal direction makes the case really sensitive to multiblock

boundary closures and breaks the preferred direction which could exists in the used grids. In order to do not repeat same conclusions as for the linear cases, the number of meshes used for this non-linear case is reduced. The notations of methods on figures are unchanged.

Something noteworthy is the fact that the initial solution in this case is not simply the point-wise values at the cells centers but really the cell-averaged values of the analytical initial solution. This was not necessary when dealing with linear convection since, because of the linearity, the point-wise values could be seen as cell-averaged values of, of course, a different initial solution. Since in the non-linear case, the solved equations are, without any approximation, equations on cell-averaged values, using point-wise values as cell-averaged values is a supplementary source of errors. This is an important point to get the right order of accuracy of the methods.

5.2.1. Effective order of accuracy

Numerical orders of the scheme have been retrieved on uniform cartesian and uniform wavy meshes: UNIF, WAVY I and WAVY II. The numerical errors presented are computed using the u and v fields. Actually, it is the sum of the L_2-error over the two fields. The errors are presented in Tables 8–10 and Fig. 27. For sake of clarity, for WAVY I and WAVY II meshes only the CART46, CUR46 and COMP46 errors have been reported on graphs.

On uniform cartesian grids, the schemes are, on average, at least fifth-order accurate. On wavy grids, in general, the errors made with CURxxx methods are inferior to those made with other schemes. One can notice that for CURxxx methods, the

Table 8
Numerical mean errors and orders of schemes on UNIF meshes for the vortex convection.

Mesh size	CART46		CART456	
	Error	Order	Error	Order
16×16	2.57×10^{-5}	–	1.85×10^{-5}	–
32×32	5.79×10^{-7}	5.47	3.51×10^{-7}	5.71
64×64	1.04×10^{-8}	5.79	6.22×10^{-9}	5.81
128×128	2.57×10^{-10}	5.33	2.18×10^{-10}	4.83

Table 9
Numerical mean errors and orders of schemes on WAVY I meshes for the vortex convection.

Mesh size	CART46		CUR46		COMP46	
	Error	Order	Error	Order	Error	Order
16×16	6.11×10^{-5}	–	4.23×10^{-5}	–	6.11×10^{-5}	–
32×32	1.17×10^{-6}	5.70	7.12×10^{-7}	5.89	9.97×10^{-7}	5.93
64×64	2.90×10^{-8}	5.33	1.26×10^{-8}	5.82	2.21×10^{-8}	5.49
128×128	9.51×10^{-10}	4.93	2.93×10^{-10}	5.42	9.13×10^{-10}	4.59

Mesh size	CART456		CUR456	
	Error	Order	Error	Order
16×16	6.37×10^{-5}	–	4.27×10^{-5}	–
32×32	4.62×10^{-7}	7.10	4.61×10^{-7}	6.53
64×64	1.50×10^{-8}	4.94	7.56×10^{-9}	5.93
128×128	8.45×10^{-10}	4.14	2.39×10^{-10}	4.98

Table 10
Numerical mean errors and orders of schemes on WAVY II meshes for the vortex convection.

Mesh size	CART46F80.49		CUR46F80.49-NORM-W2		COMP46	
	Error	Order	Error	Order	Error	Order
16×16	6.04×10^{-5}	–	3.22×10^{-5}	–	3.67×10^{-5}	–
32×32	2.39×10^{-5}	1.33	1.15×10^{-5}	1.48	2.71×10^{-5}	0.43
64×64	1.33×10^{-6}	4.17	3.41×10^{-7}	5.07	1.51×10^{-6}	4.16
128×128	1.58×10^{-8}	6.39	3.13×10^{-9}	6.76	1.59×10^{-8}	6.56
256×256	5.76×10^{-10}	4.77	9.91×10^{-11}	4.98	7.79×10^{-10}	4.35

Mesh size	CART456F80.49		CUR46F80.49-NORM-W2	
	Error	Order	Error	Order
16×16	6.04×10^{-5}	–	3.47×10^{-5}	–
32×32	2.36×10^{-5}	1.35	1.17×10^{-5}	1.56
64×64	1.27×10^{-6}	4.21	4.05×10^{-7}	4.85
128×128	1.31×10^{-8}	6.59	3.76×10^{-9}	6.75
256×256	5.61×10^{-10}	4.54	1.01×10^{-10}	5.21

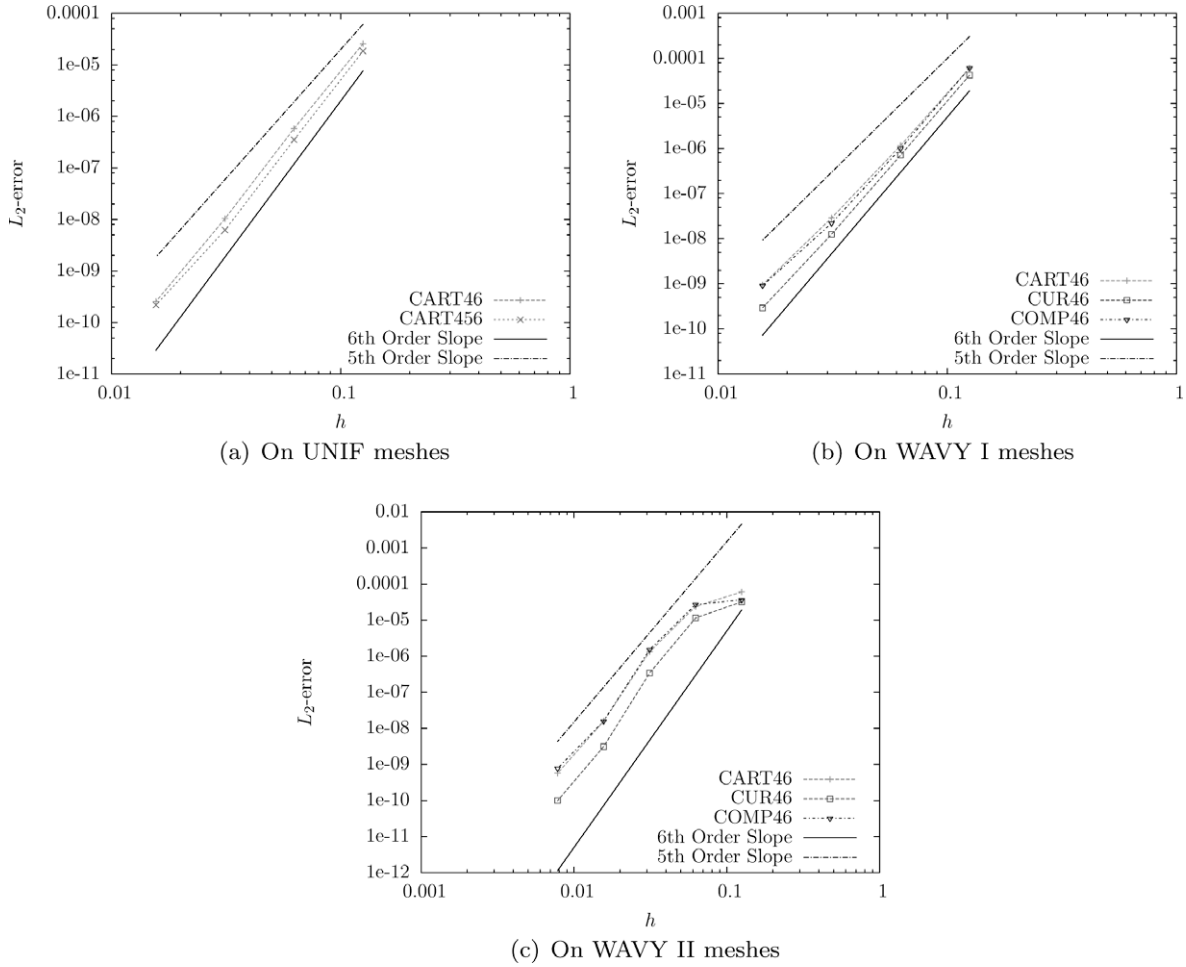

Fig. 27. Evolution of the errors following the mesh size for the 2D vortex convection.

error is at least close to 5 while for other schemes, it could decrease near to 4. However, the error is higher than the second-order expected and taking into account remarks made in Section 3 could improve these results.

5.2.2. Stability, dissipation and dispersion properties

The vortex position is captured after 25 periods for two types of meshes: WAVY III and RAND.

The results obtained on the RAND grid (Fig. 28) and on the WAVY III grid (Fig. 29) confirm conclusions of the linear convection study. The CURxxx schemes have a better behaviour than the CARTxxx and COMP46 schemes.

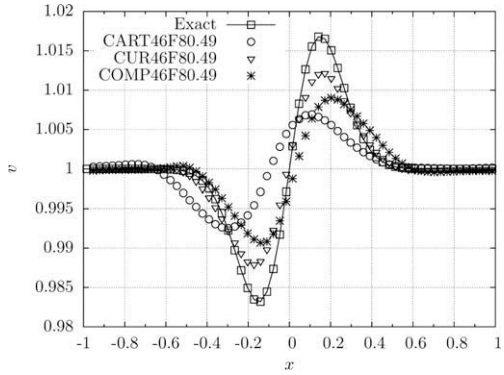

Fig. 28. $y = 0$ profile of the v-component of a vortex velocity on a RAND mesh after 25 periods.

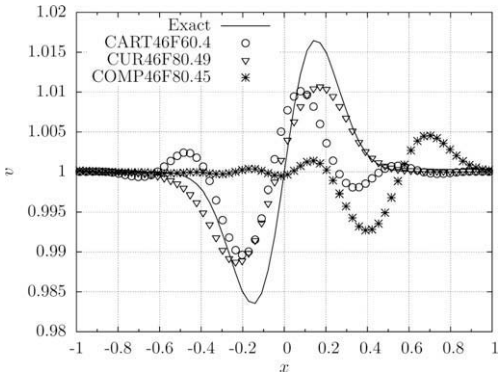

Fig. 29. $y = 0$ profile of the v-component of a vortex velocity on a WAVY III mesh after 25 periods: the CUR46 method uses the GEN frame.

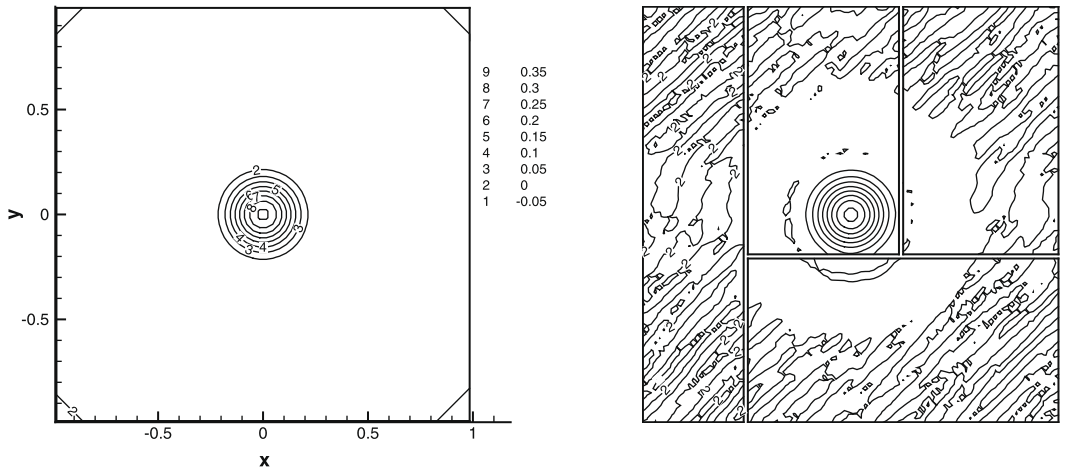

(a) Exact solution

5.2.3. Multiblock computations

Some multiblock simulations have been performed using four blocks with the CARTxxx and CURxxx schemes. Fig. 30 shows both the initial and after 50 periods isocontours of vorticity on a UNIF mesh and a WAVY II mesh. It shows that

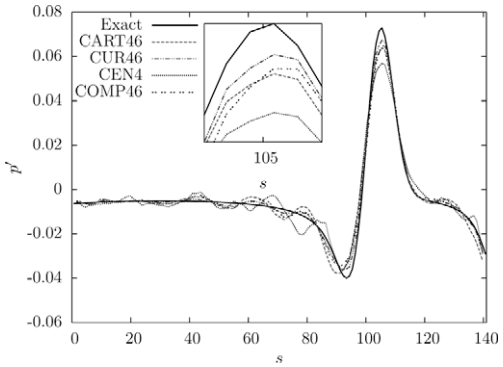

Fig. 33. Profile of the acoustic pressure along the axis $x = y$ at $t = 100$: all methods are combined with the F80.49 filter.

The inflow characteristic boundary condition of Poinsot and Lele [20] is used. The outflow boundaries are computed using Tam and Dong [24] acoustic radiative condition. Numerical results are compared with the exact solution.

A profile of the acoustic pressure along the axis $x = y$ is shown in Fig. 33. CUR46 and COMP46 schemes behave better than CART46 and CEN4 schemes. CUR46 scheme is slightly better than COMP46 in term of dissipation. CEN4 is obviously the worst schemes.

The test case was pretty difficult since it has been realized using a non-linear code while it is generally realized using linearized Euler equations. The success of the test confirms that the schemes are able to propagate properly an acoustic wave of 10^{-5} magnitude lower than the aerodynamic pressure.

6. Conclusion

High-order compact interpolation methods have been presented in order to develop high-order finite-volumes methods using small stencils on arbitrary curvilinear schemes. The first approach (CARTxxx methods) is a 1D-like scheme considering a mesh line as a 1D direction and using the curvilinear abscissa on this mesh line. The second approach (CURxxx), more general, uses supplementary cells to account for transverse derivatives terms and kinetic moments to account for the cells shape and size. This latter approach is developed in a local frame and is sixth-order in a preferred direction of this local frame. It is worth noting that both approaches match on cartesian grids. Considering parallel calculations requirements, three boundary closures for multiblock or periodic boundaries have been studied and two have been chosen for implementation in the solver **elsA**. The boundary closure which uses an upwind formulation of the flux at the second interface shows a good behaviour in terms of stability and dispersion on cartesian grids. This is no longer the case on curvilinear grids. This fact shows some limits of generalizing a 1D theoretical analysis to multidimensional problems.

Numerical tests of convection have been realized both in linear and non-linear cases to observe stability and dispersion properties of the different schemes. These tests have highlighted the need to stabilize the methods for long computations. This have been done using high-order compact filters in computational space. For most of the test cases done, filters behave very well although they are done in the computational space. Moreover, even with the filtering, the effective order of accuracy of schemes is, at least four for the CARTxxx methods and five for the CURxxx ones for two and three-dimensional flows.

Although the scheme using compact interpolation with constant coefficients (COMP46) behaves very well on uniform cartesian and curvilinear grids, when dealing with non-uniformities (irregularity of cells size), CARTxxx and CURxxx give much better results in terms of dispersion and dissipation. Moreover, when cells shape and mesh line directions strongly vary, CURxxx schemes are clearly superior to CARTxxx ones. These latter schemes could, in some of those cases, behaves worse than COMP46 schemes.

For CURxxx methods, it is shown that the choice of the local frame could help to get more stability, low dissipation and dispersion effects.

An acoustic scattering benchmark problem has also been solved with the proposed methods. This test has shown that the different methods can handle problems requiring high precision and good spectral resolution, and thus constitute an interesting building block for aeroacoustics applications in the future.

In the present paper, the extension to non-linear equations has been rapidly discussed but need a more deeper investigation. This work is on going. For the test cases presented, the different approaches which could be considered do not make a valuable difference. It would be interesting to analyze them using, for example, an isotropic homogenous turbulence simulation with a Large Eddy Simulation (LES) approach. Along these lines, it could be interesting to investigate if forcing the usage of supplementary cells even on cartesian grids could improve the isotropy properties of scheme and thus their ability to perform LES.

Appendix A. Sixth-order compact interpolation for a cartesian mesh

This section presents the derivation of the coefficients used for the cartesian-like scheme (Eq. (8)) which is sixth-order on a cartesian mesh. Therefore, it is assumed that the mesh is cartesian, which means that the i mesh lines follow a x' direction and the j mesh lines a y' direction such that (x',y') is an orthonormal frame. For sake of convenience, it is assumed that these directions x' and y' match with the usual coordinate directions x and y. Thus, when introducing the Taylor developments, it is not necessary to integrate over the y direction (neither over the z direction in the 3D case). Indeed, Eq. (8) leads to:

$$\begin{aligned}&\int_{-\frac{\Delta y}{2}}^{\frac{\Delta y}{2}} \left(\alpha u(x_{i-1/2,j},y)+u(x_{i+1/2,j},y)+\beta u(x_{i+3/2,j},y)\right)\mathrm{d}y\\ &\quad\approx \int_{-\frac{\Delta y}{2}}^{\frac{\Delta y}{2}} \left(a\frac{1}{h_{i-1}}\int_{x_{i-3/2,j}}^{x_{i-1/2,j}} u(x,y)\mathrm{d}x + b\frac{1}{h_i}\int_{x_{i-1/2,j}}^{x_{i+1/2,j}} u(x,y)\mathrm{d}x + c\frac{1}{h_{i+1}}\int_{x_{i+1/2,j}}^{x_{i+3/2,j}} u(x,y)\mathrm{d}x + d\frac{1}{h_{i+2}}\int_{x_{i+3/2,j}}^{x_{i+5/2,j}} u(x,y)\mathrm{d}x\right)\mathrm{d}y,\end{aligned} \tag{42}$$

where Δy is the size of the iso-meshline j following the y direction. Hence, it is sufficient to find the coefficients α, β, a, b, c, d such that:

$$\begin{aligned}\alpha u(x_{i-1/2,j},y)+u(x_{i+1/2,j},y)+\beta u(x_{i+3/2,j},y) \approx\ & a\frac{1}{h_{i-1}}\int_{x_{i-3/2,j}}^{x_{i-1/2,j}} u(x,y)\mathrm{d}x + b\frac{1}{h_i}\int_{x_{i-1/2,j}}^{x_{i+1/2,j}} u(x,y)\mathrm{d}x\\ &+ c\frac{1}{h_{i+1}}\int_{x_{i+1/2,j}}^{x_{i+3/2,j}} u(x,y)\mathrm{d}x + d\frac{1}{h_{i+2}}\int_{x_{i+3/2,j}}^{x_{i+5/2,j}} u(x,y)\mathrm{d}x.\end{aligned} \tag{43}$$

This shows that it is sufficient to derive a sixth-order approximation just in the x-direction. To do so, it is necessary to match the coefficient of the derivatives until the fifth-order derivative in the x-direction of the left and right hand sides of the approximation equation (43).

There are detailed the coefficients of the derivatives for the left hand side of Eq. (43):

$$\begin{aligned}&\text{0th order}\ :\ 1+\alpha+\beta,\\ &\text{1st order}\ \frac{\partial}{\partial x}:\ -\alpha h_i+\beta h_{i+1},\\ &\text{2nd order}\ \frac{\partial^2}{\partial x^2}:\ \frac{1}{2}\alpha h_i^2+\frac{1}{2}\beta h_{i+1}^2,\\ &\text{3rd order}\ \frac{\partial^3}{\partial x^3}:\ -\frac{1}{6}\alpha h_i^3+\frac{1}{6}\beta h_{i+1}^3,\\ &\text{4th order}\ \frac{\partial^4}{\partial x^4}:\ \frac{1}{24}\alpha h_i^4+\frac{1}{24}\beta h_{i+1}^4,\\ &\text{5th order}\ \frac{\partial^5}{\partial x^5}:\ -\frac{1}{120}\alpha h_i^5+\frac{1}{120}\beta h_{i+1}^5,\end{aligned} \tag{44}$$

where $h_{i'}=x_{i'+1/2}-x_{i'-1/2}$ is the distance between the interfaces $i'-1/2$ and $i'+1/2$.

The coefficients of the derivatives for the right hand side are:

$$\begin{aligned}&\text{0th order}:\ a+b+c+d,\\ &\text{1st order}\ \frac{\partial}{\partial x}:\ \frac{1}{2}[-a(2h_i+h_{i-1})-bh_i+ch_{i+1}+d(2h_{i+1}+h_{i+2})],\\ &\text{2nd order}\ \frac{\partial^2}{\partial x^2}:\ \frac{1}{6}\left[a\frac{1}{h_{i-1}}\left((h_i+h_{i-1})^3-h_i^3\right)+bh_i^2+ch_{i+1}^2+d\frac{1}{h_{i+2}}\left((h_{i+1}+h_{i+2})^3-h_{i+1}^3\right)\right],\\ &\text{3rd order}\ \frac{\partial^3}{\partial x^3}:\ \frac{1}{24}\left[a\frac{1}{h_{i-1}}\left(h_i^4-(h_i+h_{i-1})^4\right)-bh_i^3+ch_{i+1}^3+d\frac{1}{h_{i+2}}\left((h_{i+1}+h_{i+2})^4-h_{i+1}^4\right)\right],\\ &\text{4th order}\ \frac{\partial^4}{\partial x^4}:\ \frac{1}{120}\left[a\frac{1}{h_{i-1}}\left((h_i+h_{i-1})^5-h_i^5\right)+bh_i^4+ch_{i+1}^4+d\frac{1}{h_{i+2}}\left((h_{i+1}+h_{i+2})^5-h_{i+1}^5\right)\right],\\ &\text{5th order}\ \frac{\partial^5}{\partial x^5}:\ \frac{1}{720}\left[a\frac{1}{h_{i-1}}\left(h_i^6-(h_i+h_{i-1})^6\right)-bh_i^5+ch_{i+1}^5+d\frac{1}{h_{i+2}}\left((h_{i+1}+h_{i+2})^6-h_{i+1}^6\right)\right].\end{aligned} \tag{45}$$

Solving the system results in finding the following coefficients:

$$\alpha=\frac{h_{i+1}^2(h_{i-1}+h_i)(h_{i+1}+h_{i+2})}{h_{i-1}(h_i+h_{i+1})^2(h_i+h_{i+1}+h_{i+2})}, \tag{46}$$

$$\beta=\frac{h_i^2(h_{i-1}+h_i)(h_{i+1}+h_{i+2})}{(h_i+h_{i+1})^2(h_{i-1}+h_i+h_{i+1})h_{i+2}}, \tag{47}$$

$$a=\frac{h_i^2h_{i+1}^2(h_{i+1}+h_{i+2})}{h_{i-1}(h_{i-1}+h_i)(h_{i-1}+h_i+h_{i+1})^2(h_{i-1}+h_i+h_{i+1}+h_{i+2})}, \tag{48}$$

$$b=\frac{h_{i+1}^2}{h_{i-1}^2}\left(\frac{2h_{i-1}h_i(h_{i-1}+h_i)}{(h_i+h_{i+1})^3}+\frac{(2h_{i-1}-h_i)(h_{i-1}+h_i)}{(h_i+h_{i+1})^2}+\frac{h_i^3}{(h_{i-1}+h_i)(h_{i-1}+h_i+h_{i+1})^2}-\frac{h_{i-1}h_i^2(h_{i-1}+h_i)}{(h_i+h_{i+1})^2(h_{i-1}+h_i+h_{i+1})^2}\right.$$
$$\left.+\frac{h_i(h_{i-1}+h_i)(h_i(h_i+h_{i+1})-h_{i-1}(3h_i+h_{i+1}))}{(h_i+h_{i+1})^3(h_i+h_{i+1}+h_{i+2})}-\frac{h_i^3}{(h_{i-1}+h_i+h_{i+1})^2(h_{i-1}+h_i+h_{i+1}+h_{i+2})}\right), \tag{49}$$

$$c=\frac{h_i^2}{h_{i+2}^2}\left(\frac{2h_{i+2}h_{i+1}(h_{i+1}+h_{i+2})}{(h_i+h_{i+1})^3}+\frac{(-h_{i+1}+2h_{i+2})(h_{i+1}+h_{i+2})}{(h_i+h_{i+1})^2}+\frac{h_{i+1}^3}{(h_{i+1}+h_{i+2})(h_i+h_{i+1}+h_{i+2})^2}-\frac{h_{i+1}^2h_{i+2}(h_{i+1}+h_{i+2})}{(h_i+h_{i+1})^2(h_i+h_{i+1}+h_{i+2})^2}\right.$$
$$\left.+\frac{h_{i+1}(h_{i+1}+h_{i+2})(h_{i+1}(h_i+h_{i+1})-(h_i+3h_{i+1})h_{i+2})}{(h_i+h_{i+1})^3(h_{i-1}+h_i+h_{i+1})}-\frac{h_{i+1}^3}{(h_i+h_{i+1}+h_{i+2})^2(h_{i-1}+h_i+h_{i+1}+h_{i+2})}\right), \tag{50}$$

$$d=\frac{h_i^2h_{i+1}^2(h_{i-1}+h_i)}{h_{i+2}(h_{i+1}+h_{i+2})(h_i+h_{i+1}+h_{i+2})^2(h_{i-1}+h_i+h_{i+1}+h_{i+2})}. \tag{51}$$

Appendix B. Sixth-order compact interpolation for a curvilinear mesh

In this section, considering Eq. (5), details are presented about how the coefficients of the curvilinear scheme using transverse derivatives and local frame are determined. For sake of simplicity all developments are done for the 2D case. For sake of convenience the local reference frame (x',y') is assumed to match with the usual frame (x,y). All equations written there are retrieved in (x',y') just by replacing x and y by x' and y' respectively. The interpolation is done around the interface $(i+1/2,j)$. There are some definitions on an interface $(i'+1/2,j')$:

$$x_{i'+1/2,j'}=\frac{1}{S_{i'+1/2,j'}}\int_{S_{i'+1/2,j'}}x\,\mathrm{d}S,$$
$$y_{i'+1/2,j'}=\frac{1}{S_{i'+1/2,j'}}\int_{S_{i'+1/2,j'}}y\,\mathrm{d}S,$$
$$J^{x^ny^m}_{i'+1/2,j'}=\frac{1}{S_{i'+1/2,j'}}\int_{S_{i'+1/2,j'}}(x-x_{i'+1/2})^n(y-y_{i'+1/2})^m\,\mathrm{d}S,$$
$$\delta^x_{i'+1/2,j'}=x_{i'+1/2,j'}-x_{i+1/2,j},$$
$$\delta^y_{i'+1/2,j'}=y_{i'+1/2,j'}-y_{i+1/2,j}.$$

Since, just interfaces on the jth i mesh line are considered, interfaces underscripts are just $i'+1/2$ instead of $(i'+1/2,j)$. With same considerations, coefficients $\alpha_{i+1/2,j,k}$, $\beta_{i+1/2,j,k}$, and $a^{i+1/2,j,k}_{\cdot,\cdot,\cdot}$ are just noted α,β, and $a_{\cdot,\cdot,\cdot}$. There are now equivalent definitions for a cell (i,j):

$$x_{i',j'}=\frac{1}{V_{i',j'}}\int_{V_{i',j'}}x\,\mathrm{d}V,$$
$$y_{i',j'}=\frac{1}{V_{i',j'}}\int_{V_{i',j'}}y\,\mathrm{d}V,$$
$$J^{x^ny^m}_{i',j'}=\frac{1}{V_{i',j'}}\int_{V_{i',j'}}(x-x_{i',j'})^n(y-y_{i',j'})^m\,\mathrm{d}V,$$
$$\delta^x_{i',j'}=x_{i',j'}-x_{i+1/2},$$
$$\delta^y_{i',j'}=y_{i',j'}-y_{i+1/2}.$$

One can note that $J^x_{\cdots}=J^y_{\cdots}=0$.

The Taylor series of a function $u(x,y)$ at the point (x_0,y_0) is

$$u(x,y)=\sum_{m=0}^{\infty}\sum_{n=0}^{\infty}\frac{\partial^{m+n}}{\partial x^m\partial y^n}u(x_0,y_0)\frac{1}{m!}\frac{1}{n!}(x-x_0)^m(y-y_0)^n. \tag{52}$$

So, the mean value of u on a domain Ω is

$$\bar{u}_\Omega=\frac{1}{|\Omega|}\int_\Omega u\,\mathrm{d}\Omega=\frac{1}{|\Omega|}\int_\Omega\left[\sum_{m=0}^{\infty}\sum_{n=0}^{\infty}\frac{\partial^m}{\partial x^m}\frac{\partial^n}{\partial y^n}u(x_0,y_0)\frac{1}{m!}\frac{1}{n!}(x-x_0)^m(y-y_0)^n\right]\mathrm{d}\Omega. \tag{53}$$

When introducing Taylor series around $x_{i+1/2}$, on the left hand side, coefficients of the derivatives which will be cancelled are:

$$
\begin{aligned}
&\text{0th order}: \ 1+\alpha+\beta,\\
&\text{1st order}\frac{\partial}{\partial x}: \ \alpha\delta^x_{i-1/2}+\beta\delta^x_{i+3/2},\\
&\frac{\partial}{\partial y}: \ \alpha\delta^y_{i-1/2}+\beta\delta^y_{i+3/2},\\
&\text{2nd order}\frac{\partial^2}{\partial x^2}: \ \frac{1}{2}\alpha\left((\delta^x_{i-1/2})^2+J^{x^2}_{i-1/2}\right)+\frac{1}{2}J^{x^2}_{i+1/2}+\frac{1}{2}\beta\left((\delta^x_{i+3/2})^2+J^{x^2}_{i+3/2}\right),\\
&\frac{\partial^2}{\partial y^2}: \ \frac{1}{2}\alpha\left((\delta^y_{i-1/2})^2+J^{y^2}_{i-1/2}\right)+\frac{1}{2}J^{y^2}_{i+1/2}+\frac{1}{2}\beta\left((\delta^y_{i+3/2})^2+J^{y^2}_{i+3/2}\right),\\
&\frac{\partial^2}{\partial x\partial y}: \ \alpha\left(\delta^x_{i-1/2}\delta^y_{i-1/2}+J^{xy}_{i-1/2}\right)+J^{xy}_{i+1/2}+\beta\left(\delta^x_{i+3/2}\delta^y_{i+3/2}+J^{xy}_{i+3/2}\right),\\
&\text{3rd order}\frac{\partial^3}{\partial x^3}: \ \frac{1}{6}\alpha\left((\delta^x_{i-1/2})^3+3\delta^x_{i-1/2}J^{x^2}_{i-1/2}+J^{x^3}_{i-1/2}\right)+\frac{1}{6}J^{x^3}_{i+1/2}+\frac{1}{6}\beta\left((\delta^x_{i+3/2})^3+3\delta^x_{i+3/2}J^{x^2}_{i+3/2}+J^{x^3}_{i+3/2}\right),\\
&\frac{\partial^3}{\partial y^3}: \ \frac{1}{6}\alpha\left((\delta^y_{i-1/2})^3+3\delta^y_{i-1/2}J^{y^2}_{i-1/2}+J^{y^3}_{i-1/2}\right)+\frac{1}{6}J^{y^3}_{i+1/2}+\frac{1}{6}\beta\left((\delta^y_{i+3/2})^3+3\delta^y_{i+3/2}J^{y^2}_{i+3/2}+J^{y^3}_{i+3/2}\right),\\
&\frac{\partial^3}{\partial x^2\partial y}: \ \frac{1}{2}\alpha\left((\delta^x_{i-1/2})^2\delta^y_{i-1/2}+2\delta^x_{i-1/2}J^{xy}_{i-1/2}+\delta^y_{i-1/2}J^{x^2}_{i-1/2}+J^{x^2y}_{i-1/2}\right)+\frac{1}{2}J^{x^2y}_{i+1/2}+\frac{1}{2}\beta\left((\delta^x_{i+3/2})^2\delta^y_{i+3/2}\right.\\
&\qquad\left.+2\delta^x_{i+3/2}J^{xy}_{i+3/2}+\delta^y_{i+3/2}J^{x^2}_{i+3/2}+J^{x^2y}_{i+3/2}\right),\\
&\frac{\partial^3}{\partial x\partial y^2}: \ \frac{1}{2}\alpha\left(\delta^x_{i-1/2}(\delta^y_{i-1/2})^2+2\delta^y_{i-1/2}J^{xy}_{i-1/2}+\delta^x_{i-1/2}J^{y^2}_{i-1/2}+J^{xy^2}_{i-1/2}\right)\\
&\qquad+\frac{1}{2}J^{xy^2}_{i+1/2}+\frac{1}{2}\beta\left(\delta^x_{i+3/2}(\delta^y_{i+3/2})^2+2\delta^y_{i+3/2}J^{xy}_{i+3/2}+\delta^x_{i+3/2}J^{y^2}_{i+3/2}+J^{xy^2}_{i+3/2}\right),\\
&\text{4th order transverse terms will not be used}\\
&\frac{\partial^4}{\partial x^4}: \ \frac{1}{24}\alpha\left((\delta^x_{i-1/2})^4+6(\delta^x_{i-1/2})^2J^{x^2}_{i-1/2}+4\delta^x_{i-1/2}J^{x^3}_{i-1/2}+J^{x^4}_{i-1/2}\right)\\
&\qquad+\frac{1}{24}J^{x^4}_{i+1/2}+\frac{1}{24}\beta\left((\delta^x_{i+3/2})^4+6(\delta^x_{i+3/2})^2J^{x^2}_{i+3/2}+4\delta^x_{i+3/2}J^{x^3}_{i+3/2}+J^{x^4}_{i+3/2}\right),\\
&\text{5th order transverse terms will not be used}\\
&\frac{\partial^5}{\partial x^5}: \ \frac{1}{120}\alpha\left((\delta^x_{i-1/2})^5+10(\delta^x_{i-1/2})^3J^{x^2}_{i-1/2}+10(\delta^x_{i-1/2})^2J^{x^3}_{i-1/2}+5\delta^x_{i-1/2}J^{x^4}_{i-1/2}+J^{x^5}_{i-1/2}\right)+\frac{1}{120}J^{x^5}_{i+1/2}\\
&\qquad+\frac{1}{120}\beta\left((\delta^x_{i+3/2})^5+10(\delta^x_{i+3/2})^3J^{x^2}_{i+3/2}+10(\delta^x_{i+3/2})^2J^{x^3}_{i+3/2}+5\delta^x_{i+3/2}J^{x^4}_{i+3/2}+J^{x^5}_{i+3/2}\right).
\end{aligned}
$$

On the right hand side, the following coefficients are found:

$$
\begin{aligned}
&\text{0th order}: \ \sum_{l=-m}^{l=n}\sum_{p=-q}^{p=r}a_{l,p},\\
&\text{1st order}: \frac{\partial}{\partial x}: \ \sum_{l=-m}^{l=n}\sum_{p=-q}^{p=r}a_{l,p}\delta^x_{i+l,j+p},\\
&\frac{\partial}{\partial y}: \ \sum_{l=-m}^{l=n}\sum_{p=-q}^{p=r}a_{l,p}\delta^y_{i+l,j+p},\\
&\text{2nd order} \ \frac{\partial^2}{\partial x^2}: \frac{1}{2}\sum_{l=-m}^{l=n}\sum_{p=-q}^{p=r}a_{l,p}\left((\delta^x_{i+l,j+p})^2+J^{x^2}_{i+l,j+p}\right),\\
&\frac{\partial^2}{\partial y^2}: \frac{1}{2}\sum_{l=-m}^{l=n}\sum_{p=-q}^{p=r}a_{l,p}\left((\delta^y_{i+l,j+p})^2+J^{y^2}_{i+l,j+p}\right),\\
&\frac{\partial^2}{\partial x\partial y}: \ \sum_{l=-m}^{l=n}\sum_{p=-q}^{p=r}a_{l,p}\left(\delta^x_{i+l,j+p}\delta^y_{i+l,j+p}+J^{xy}_{i+l,j+p}\right),
\end{aligned}
$$

(54)

3rd order $\frac{\partial^3}{\partial x^3}: \frac{1}{6}\sum_{l=-m}^{l=n}\sum_{p=-q}^{p=r} a_{l,p}\left((\delta^x_{i+l,j+p})^3 + 3\delta^x_{i+l,j+p}J^{x^2}_{i+l,j+p} + J^{x^3}_{i+l,j+p}\right)$,

$\frac{\partial^3}{\partial y^3}: \frac{1}{6}\sum_{l=-m}^{l=n}\sum_{p=-q}^{p=r} a_{l,p}\left((\delta^y_{i+l,j+p})^3 + 3\delta^y_{i+l,j+p}J^{y^2}_{i+l,j+p} + J^{y^3}_{i+l,j+p}\right)$,

$\frac{\partial^3}{\partial x^2\partial y}: \frac{1}{2}\sum_{l=-m}^{l=n}\sum_{p=-q}^{p=r} a_{l,p}\left((\delta^x_{i+l,j+p})^2\delta^y_{i+l,j+p} + 2\delta^x_{i+l,j+p}J^{xy}_{i+l,j+p} + \delta^y_{i+l,j+p}J^{x^2}_{i+l,j+p} + J^{x^2y}_{i+l,j+p}\right)$,

$\frac{\partial^3}{\partial x\partial y^2}: \frac{1}{2}\sum_{l=-m}^{l=n}\sum_{p=-q}^{p=r} a_{l,p}\left(\delta^x_{i+l,j+p}(\delta^y_{i+l,j+p})^2 + 2\delta^y_{i+l,j+p}J^{xy}_{i+l,j+p} + \delta^x_{i+l,j+p}J^{y^2}_{i+l,j+p} + J^{xy^2}_{i+l,j+p}\right)$,

4th order transverse terms will not be used

$\frac{\partial^4}{\partial x^4}: \frac{1}{24}\sum_{l=-m}^{l=n}\sum_{p=-q}^{p=r} a_{l,p}\left((\delta^x_{i+l,j+p})^4 + 6(\delta^x_{i+l,j+p})^2J^{x^2}_{i+l,j+p} + 4\delta^x_{i+l,j+p}J^{x^3}_{i+l,j+p} + J^{x^4}_{i+l,j+p}\right)$,

5th order transverse terms will not be used

$$\frac{\partial^5}{\partial x^5}: \frac{1}{120}\sum_{l=-m}^{l=n}\sum_{p=-q}^{p=r} a_{l,p}\left((\delta^x_{i+l,j+p})^5 + 10(\delta^x_{i+l,j+p})^3J^{x^2}_{i+l,j+p} + 10(\delta^x_{i+l,j+p})^2J^{x^3}_{i+l,j+p} + 5\delta^x_{i+l,j+p}J^{x^4}_{i+l,j+p} + J^{x^5}_{i+l,j+p}\right). \quad (55)$$

It is now necessary to prove that this method matches with the cartesian-like method when a cartesian grid is considered. To do so, for sake of simplicity, let be considered a 2D case with notations introduced in Section 2.2.3 and in Appendix A. It is clear that the three types of local reference frames introduced are the same in this case. It is still assumed that the preferred direction for the interface $(i+1/2,j)$ is the x direction. The aim is to show that the coefficients $X = (\underbrace{\alpha,\beta,a,b,c,d}_{X_1},\underbrace{e,f,g,h}_{X_2})$ with α, β, a, b, c, d defined as in Appendix A and $e=f=g=h=0$ is the one which verify the equations defined for the CURxxx method.

Considering that coefficients α, β, a, b, c, d are determined by matching coefficients of derivatives in the x directions involving in Eq. (42), it is clear that:

$$(A \quad B)X = 0.$$

This could be checked using the following expressions of kinetic moments:

$\delta^x_{i-1/2,j} = -h_i$ and $\delta^y_{i-1/2,j} = 0$

$\delta^x_{i+3/2,j} = h_{i+1}$ and $\delta^y_{i+3/2,j} = 0$

$J^{x^my^n}_{i-1/2,j} = J^{x^my^n}_{i+1/2,j} = J^{x^my^n}_{i+3/2,j} = 0, \quad \forall m > 0$

$J^{y^2}_{i-1/2,j} = J^{y^2}_{i+1/2,j} = J^{y^2}_{i+3/2,j} = \Delta y^2/12$

$J^{y^3}_{i-1/2,j} = J^{y^3}_{i+1/2,j} = J^{y^3}_{i+3/2,j} = 0$

$\delta^x_{i-1,j} = -(h_{i-1}/2 + h_i), \quad \delta^x_{i,j} = -h_i/2, \quad \delta^x_{i+1,j} = h_{i+1}/2$ and $\delta^x_{i+2,j} = (h_{i+1} + h_{i+2}/2)$,

$\delta^y_{i-1,j} = \delta^y_{i,j} = \delta^y_{i+1,j} = \delta^y_{i+2,j} = 0$,

$J^{x^my^n}_{i-1,j} = J^{x^my^n}_{i,j} = J^{x^my^n}_{i+1,j} = J^{x^my^n}_{i+2,j} = 0$, $\forall m,n$ if m or n is odd,

$J^{x^2}_{i-1,j} = h^2_{i-1}/12, \quad J^{x^2}_{i,j} = h^2_i/12, \quad J^{x^2}_{i+1,j} = h^2_{i+1}/12$ and $J^{x^2}_{i+2,j} = h^2_{i+2}/12$,

$J^{x^4}_{i-1,j} = h^4_{i-1}/80, \quad J^{x^4}_{i,j} = h^4_i/80, \quad J^{x^4}_{i+1,j} = h^4_{i+1}/80$ and $J^{x^4}_{i+2,j} = h^4_{i+2}/80$,

$J^{x^5}_{i-1,j} = J^{x^5}_{i,j} = J^{x^5}_{i+1,j} = J^{x^5}_{i+2,j} = 0$,

$J^{y^2}_{i-1,j} = J^{y^2}_{i,j} = J^{y^2}_{i+1,j} = J^{y^2}_{i+2,j} = \Delta y^2/12$,

$J^{y^4}_{i-1,j} = J^{y^4}_{i,j} = J^{y^4}_{i+1,j} = J^{y^4}_{i+2,j} = \Delta y^4/80$,

where Δy is the length following the y direction of the interface $(i+1/2,j)$. It could also be checked that the given vector X verify all the relations given by the transverse derivatives. Indeed, the following relations are obtained:

$$\frac{\partial}{\partial y}\colon\ 0 = e\delta^y_{ij-1} + f\delta^y_{ij+1} + g\delta^y_{i+1j-1} + h\delta^y_{i+1j+1},$$

$$\frac{\partial^2}{\partial y^2}\colon\ \frac{\Delta y^2}{24}(\alpha+1+\beta) = \frac{\Delta y^2}{24}(a+b+c+d) + \frac{1}{2}e((\delta^y_{ij-1})^2 + J^{y^2}_{ij-1}) + \frac{1}{2}f((\delta^y_{ij+1})^2 + J^{y^2}_{ij+1}) + \frac{1}{2}g((\delta^y_{i+1j-1})^2 + J^{y^2}_{i+1j-1}) + \frac{1}{2}h((\delta^y_{ij-1})^2 + J^{y^2}_{i+1j+1}),$$

$$\frac{\partial^2}{\partial x\partial y}\colon\ 0 = e(\delta^x_{ij-1}\delta^y_{ij-1} + J^{xy}_{ij-1}) + f(\delta^x_{ij+1}\delta^y_{ij+1} + J^{xy}_{ij+1}) + g(\delta^x_{i+1j-1}\delta^y_{i+1j-1} + J^{xy}_{i+1j-1}) + h(\delta^x_{i+1j+1}\delta^y_{i+1j+1} + J^{xy}_{i+1j+1}),$$

$$\frac{\partial^3}{\partial y^3}\colon\ 0 = \frac{1}{6}e((\delta^y_{ij-1})^3 + 3\delta^y_{ij-1}J^{y^2}_{ij-1}) + \frac{1}{6}f((\delta^y_{ij+1})^3 + 3\delta^y_{ij+1}J^{y^2}_{ij+1}) + \frac{1}{6}g((\delta^y_{i+1j-1})^3 + 3\delta^y_{i+1j-1}J^{y^2}_{i+1j-1}) +$$
$$\frac{1}{6}h((\delta^y_{i+1j+1})^3 + 3\delta^y_{i+1j+1}J^{y^2}_{i+1j+1}),$$

$$\frac{\partial^3}{\partial x^2\partial y}\colon\ 0 = \frac{1}{2}e((\delta^x_{ij-1})^2\delta^y_{ij-1} + \delta^y_{ij-1}J^{x^2}_{ij-1}) + \frac{1}{2}f((\delta^x_{ij+1})^2\delta^y_{ij+1} + \delta^y_{ij+1}J^{x^2}_{ij+1}) + \frac{1}{2}g((\delta^x_{i+1j-1})^2\delta^y_{i+1j-1}$$
$$+\delta^y_{i+1j-1}J^{x^2}_{i+1j-1}) + \frac{1}{2}h((\delta^x_{i+1j+1})^2\delta^y_{i+1j+1} + \delta^y_{i+1j+1}J^{x^2}_{i+1j+1}),$$

$$\frac{\partial^3}{\partial x\partial y^2}\colon\ 0 = \frac{1}{2}e\left(\delta^x_{ij-1}(\delta^y_{ij-1})^2 + \delta^x_{ij-1}J^{y^2}_{ij-1}\right)$$
$$\frac{1}{2}f\left(\delta^x_{ij+1}(\delta^y_{ij+1})^2 + \delta^x_{ij+1}J^{y^2}_{ij+1}\right)$$
$$\frac{1}{2}g\left(\delta^x_{i+1j-1}(\delta^y_{i+1j-1})^2 + \delta^x_{i+1j-1}J^{y^2}_{i+1j-1}\right)$$
$$\frac{1}{2}h\left(\delta^x_{i+1j+1}(\delta^y_{i+1j+1})^2 + \delta^x_{i+1j+1}J^{y^2}_{i+1j+1}\right).$$

Solving these equations by a least square method leads to zero values for e, f, g and h.

Appendix C. Computation of kinetic moments

This section presents the calculation of kinetic moment which are used in the formulation of interpolation coefficients. Firstly, these moments are pre-computed in the general frame and geometrical transformations are then employed to obtain these moments in local frame. Unfortunately, this method suffers of round-off errors if the mesh is very-stretched, therefore the calculation of kinetic moments is done directly in local frame.

The coordinates in global frame are denoted as (x,y,z), and as (x',y',z') for the local frame. Two kind of moments have to be calculated: cells and interfaces kinetic moments. Cells kinetic moments are denoted by $J^{x'^m y'^n z'^p}$. Since the local coordinate x', y', z' could be expressed as linear function of x, y, z, the calculation of kinetic moments consist simply of the numerical integration of polynomial function:

$$J^{x'^m y'^n z'^p} = \frac{1}{|\Omega|}\int_\Omega \left[\underbrace{(a_{x'}a + b_{x'}y + c_{x'}z + d_{x'})^m}_{x'} \ldots \underbrace{(a_{z'}x + b_{z'}y + c_{z'}z + d_{z'})^p}_{z'}\right] d\Omega = \frac{1}{|\Omega|}\int_\Omega P(x,y,z)\,d\Omega \tag{56}$$

where $P(x,y,z)$ represent a polynomial of order $n+m+p$ function of x, y, z.

The cell Ω is supposed to be defined only by its eight vertices, and a tri-linear transformation is applied to transform the physical cell Ω into the iso-parametric cell Ω^* defined by:

$$\Omega^* = \begin{cases} -1 \leqslant \xi \leqslant 1 \\ -1 \leqslant \eta \leqslant 1 \\ -1 \leqslant \zeta \leqslant 1 \end{cases}, \tag{57}$$

and the numerical integration is performed by a Gauss quadrature on Ω^*.

The position vector for a point inside the cell Ω can be expressed in terms of ξ, η and ζ by:

$$\begin{aligned} 8\vec{x} = {} & (1-\xi)(1-\eta)(1-\zeta)\vec{x_1} + (1+\xi)(1-\eta)(1-\zeta)\vec{x_2} + (1-\xi)(1+\eta)(1-\zeta)\vec{x_3} + (1+\xi)(1+\eta)(1-\zeta)\vec{x_4} \\ & + (1-\xi)(1-\eta)(1+\zeta)\vec{x_5} + (1+\xi)(1-\eta)(1+\zeta)\vec{x_6} + (1-\xi)(1+\eta)(1+\zeta)\vec{x_7} + (1+\xi)(1+\eta)(1+\zeta)\vec{x_8}, \end{aligned} \tag{58}$$

where $\vec{x_i}$ represent the vertices of Ω. Thus we obtain:

$$J^{x'^m y'^n z'^p} = \frac{1}{|\Omega|}\int_{-1}^{1}\int_{-1}^{1}\int_{-1}^{1} |Jac| P(\xi,\eta,\zeta)\,d\xi\,d\eta\,d\zeta, \tag{59}$$

where $|Jac|$ denote the jacobian of the tri-linear transformation.

A Gaussian approximation is used for each integral:

$$J^{x'^m y'^n z'^p} = \frac{1}{|\Omega|}\sum\sum\sum w_i w_j w_k |Jac| P(\beta_i,\beta_j,\beta_k), \tag{60}$$

where β_i represent the Gauss points and w_i the corresponding weight. As the highest order for kinetic moments integrands is five, the highest order is six for the function $|Jac|P$ and so three Gauss points are used in each direction.

One can notice that the grid geometry can be approximated to a higher order by using a polynomial transformation instead of a tri-linear ones. This possibility will be studied in the future.

For an interface kinetic moment, a parametrization of the interface is introduced as for the cell moment and the formula:

$$\int_S f(x,y,z)dS = \int_{-1}^{1}\int_{-1}^{1} f(\xi,\eta)\|\vec{r}_\xi\vec{r}_\eta\|d\xi\,d\eta \tag{61}$$

is used to calculate the integral with a Gaussian quadrature. In this formula, $\vec{r}(\xi,\eta)$ represent a point on the surface S and the two vector $\vec{r}_\xi$ and $\vec{r}_\eta$ are calculated by:

$$\vec{r}_t = \left(\frac{\partial x}{\partial t}, \frac{\partial y}{\partial t}, \frac{\partial z}{\partial t}\right)^T \tag{62}$$

where t represents either ξ or η.

References

[1] G. Ashcroft, X. Zhang, Optimized prefactored compact schemes, Journal of Computational Physics 190 (2) (2003) 459–477.
[2] L. Cambier, M. Gazaix, elsA: an efficient object-oriented solution to CFD complexity, in: 40th AIAA Aerospace Science Meeting and Exhibit, Reno, AIAA 2002-0108, January 2002, pp. 14–17.
[3] D.V. Gaitonde, J.S. Shang, Optimized compact-difference-based finite-volume schemes for linear wave phenomena, Journal of Computational Physics 138 (2) (1997) 617–643.
[4] D.V. Gaitonde, M.R. Visbal, Further development of a Navier–Stokes solution procedure based on higher-order formulas, in: 37th Aerospace Sciences Meeting and Exhibit, Reno, Nevada, No. AIAA-1999-557, January 11–14 1999.
[5] L. Gamet, F. Ducros, F. Nicoud, T. Poinsot, Compact finite difference schemes on non-uniform meshes. application to direct numerical simulations of compressible flows, International Journal for Numerical Methods in Fluids 29 (1999) 159–191.
[6] X. Gloerfelt, Bruit Rayonné par un Écoulement Affleurant une Cavité: Simulation Aéroacoustique Directe et Application de Méthodes Intégrales. Ph.D. thesis, Laboratoire de Mécanique de Fluides et d'Acoustique, UMR CNRS 5509, Ecole Centrale de Lyon, Novembre 2001.
[7] S. Gottlieb, W. Chi-Shu, Total variation diminishing Runge–Kutta schemes, Tech. Rep., Institute for Computer Applications in Science and Engineering (ICASE), 1996.
[8] B. Gustafsson, The convergence rate for difference approximations to mixed initial boundary value problems, Mathematics of Computations 29 (130) (1975) 396–406.
[9] J.C. Hardin, J.R. Ristorcelli, C.K.W. Tam (Eds.), October 24–26 1994, ICASE/LaRC Workshop on Benchmark Problems in Computational Aeroacoustics (CAA), NASA and ICASE, Hampton, Virginia.
[10] R. Hixon, Prefactored small-stencil compact schemes, Journal of Computational Physics 165 (2) (2000) 522–541.
[11] A. Jameson, W. Schmidt, E. Turkel, Numerical solutions of the Euler equations by finite volume methods using Runge–Kutta time-stepping schemes, in: AIAA 14th Fluid and Plasma Dynamic Conference, No. AIAA Paper 81-1259, Palo Alto, 1981.
[12] M.H. Kobayashi, On a class of padé finite volume methods, Journal of Computational Physics 156 (1) (1999) 137–180.
[13] C. Lacor, S. Smirnov, M. Baelmans, A finite volume formulation of compact schemes on arbitrary structured grids, Journal of Computational Physics 198 (2004) 535–566.
[14] S.K. Lele, Compact finite difference schemes with spectral-like resolution, Journal of Computational Physics 103 (1992) 16–42.
[15] C. Mattiussi, An analysis of finite volume, finite element, and finite difference methods using some concepts of algebraic topology, Journal of Computational Physics 133 (2) (1997) 289–309.
[16] D.V. Nance, K. Viswanathan, L.N. Sankar, Low-dispersion finite volume scheme for aeroacoustic applications, AIAA Journal 35 (2) (1997) 255–262.
[17] J.M.C. Pereira, M.H. Kobayashi, J.C.F. Pereira, A fourth-order-accurate finite volumenext term compact method for the incompressible Navier–Stokes solutions, Journal of Computational Physics 167 (1) (2001) 217–243.
[18] M. Piller, E. Stalio, Finite-volume compact schemes on staggered grids, Journal of Computational Physics 197 (1) (2004) 299–340.
[19] M. Piller, E. Stalio, Compact finite volume schemes on boundary-fitted grids, Journal of Computational Physics 227 (9) (2008) 4736–4762.
[20] T.J. Poinsot, S.K. Lele, Boundary conditions for direct simulations of compressible viscous flows, Journal of Computational Physics 101 (1992) 104–129.
[21] M. Popescu, W. Shyy, M. Garbey, Finite volume treatment of dispersion–relation-preserving and optimized prefactored compact schemes for wave propagation, Journal of Computational Physics 210 (2) (2005) 705–729.
[22] T.K. Sengupta, G. Ganeriwal, S. De, Analysis of central and upwind compact schemes, Journal of Computational Physics 192 (2003) 677–694.
[23] C.K.W. Tam, Computational aeroacoustics: issues and methods, AIAA Journal 33 (10) (1995) 1788–1796.
[24] C.K.W. Tam, Z. Dong, Radiation and outflow boundary conditions for direct computation of acoustic and flow disturbances in a nonuniform mean flow, Journal of Computational Acoustics 4 (2) (1996) 175–201.
[25] C.K.W. Tam, J.C. Webb, Dispersion–relation-preserving finite difference schemes for computational acoustics, Journal of Computational Physics 107 (2) (1993) 262–281.
[26] M.R. Visbal, D.V. Gaitonde, On the use of higher-order finite-difference schemes on curvilinear and deforming meshes, Journal of Computational Physics 181 (1) (2002) 155–185.